Earth Syst. Sci. Data, 10, 2069–2095, 2018
https://doi.org/10.5194/essd-10-2069-2018

Open Access Earth System Science Data

The Berkeley High Resolution Tropospheric NO_2 product

Joshua L. Laughner[1,a], **Qindan Zhu**[2], **and Ronald C. Cohen**[1,2]

[1]Department of Chemistry, University of California, Berkeley, Berkeley, CA 94720, USA
[2]Department of Earth and Planetary Sciences, University of California, Berkeley, Berkeley, CA 94720, USA
[a]now at: Department of Geological and Planetary Sciences, California Institute of Technology, Pasadena, CA 91125, USA

Correspondence: Ronald C. Cohen (rccohen@berkeley.edu)

Received: 16 May 2018 – Discussion started: 25 June 2018
Revised: 9 October 2018 – Accepted: 30 October 2018 – Published: 27 November 2018

Abstract. We describe upgrades to the Berkeley High Resolution (BEHR) NO_2 satellite retrieval product. BEHR v3.0B builds on the NASA version 3 standard Ozone Monitoring Instrument (OMI) tropospheric NO_2 product to provide a high spatial resolution product for a domain covering the continental United States and lower Canada that is consistent with daily variations in the 12 km a priori NO_2 profiles. Other improvements to the BEHR v3.0 product include surface reflectance and elevation, and factors affecting the NO_2 a priori profiles such as lightning and anthropogenic emissions.

We describe the retrieval algorithm in detail and evaluate the impact of changes to the algorithm between v2.1C and v3.0B on the retrieved NO_2 vertical column densities (VCDs). Not surprisingly, we find that, on average, the changes to the a priori NO_2 profiles and the update to the new NASA slant column densities have the greatest impact on the retrieved VCDs. More significantly, we find that using daily a priori profiles results in greater average VCDs than using monthly profiles in regions and times with significant lightning activity.

The BEHR product is available as four subproducts on the University of California DASH repository, using monthly a priori profiles at native OMI pixel resolution (https://doi.org/10.6078/D1N086) and regridded to $0.05° \times 0.05°$ (https://doi.org/10.6078/D1RQ3G) and using daily a priori profiles at native OMI (https://doi.org/10.6078/D1WH41) and regridded (https://doi.org/10.6078/D12D5X) resolutions. The subproducts using monthly profiles are currently available from January 2005 to July 2017, and will be expanded to more recent years. The subproducts using daily profiles are currently available for years 2005–2010 and 2012–2014; 2011 and 2015 on will be added as the necessary input data are simulated for those years.

1 Introduction

Nitrogen oxides ($NO + NO_2 \equiv NO_x$) are trace gases in the atmosphere and are key species controlling air quality and affecting radiative balance. NO_x regulates the chemical production of tropospheric ozone (Jacob et al., 1993), which affects the radiative balance in the upper troposphere (Myhre et al., 2013) and is harmful to plants (Haagen-Smit et al., 1952; Heath, 1975), animals, and humans (Menzel, 1984) at the surface. It also plays a role in the formation of aerosol particles (Izumi and Fukuyama, 1990; Pandis et al., 1992; Carlton et al., 2009; Rollins et al., 2012), which also affect the radiative balance of the atmosphere (Boucher et al., 2013). Exposure to fine particles is also a strong factor controlling life expectancy (Dockery et al., 1993; Pope et al., 2009; Burnett et al., 2018). Additionally, NO_x itself is harmful, as, for example, exposure causes bronchoconstriction and associated difficulty breathing, especially for those affected by asthma (Kagawa, 1985; Chauhan et al., 1998; Wegmann et al., 2005; Kampa and Castanas, 2008).

NO_x is emitted from a variety of sources, both anthropogenic and natural. Anthropogenic sources typically involve combustion, including motor vehicles and fossil fuel electrical generation. Natural sources include biomass burning, lightning, and soil bacteria. Understanding all of these sources is crucial to understanding the reactive nitrogen bud-

get and predicting how future changes in emissions will affect air quality and climate change.

Satellite observations provide uniquely comprehensive spatial maps of NO_2, allowing inference of NO_x emissions. The spatial resolution available with early instruments (i.e., the Global Ozone Monitoring Experiment, GOME, $40 \times 320\,km^2$, Burrows et al., 1999; the SCanning Imaging Absorption SpectroMeter for Atmospheric CHartographY, SCIAMACHY, $30 \times 60\,km^2$, Noel et al., 1998) allowed inferences at the scale of entire continents or entire metropolitan regions, including cities and their surroundings. More recent instruments have much higher resolution (e.g., the Ozone Monitoring Instrument, OMI, $13 \times 24\,km^2$, Levelt et al., 2006; the Tropospheric Monitoring Instrument, TROPOMI, $7 \times 7\,km^2$, Veefkind et al., 2012), allowing inferences about individual point sources and urban cores. Ground based measurements sample emissions at specific points in great detail; however, extrapolating such measurements to an entire region requires assumptions that are difficult to test, such as fleet composition and operating mode (e.g., Fujita et al., 2012; Anderson et al., 2014), that can bias estimates of the total vehicle emissions from a region. Satellite observations cannot currently provide the same level of detail as a roadside measurement, but by observing the entire city, provide a top–down constraint on its total NO_x emissions that include observations on every point in the domain. Satellite observations have been used in a wide variety of applications in this vein, including direct observation of emissions and trends (e.g., Russell et al., 2012), plume analysis to derive emissions and chemical lifetime (e.g., Beirle et al., 2011; Valin et al., 2013; Lu et al., 2015; Liu et al., 2016, 2017), model constraint (e.g., Travis et al., 2016), and data assimilation (e.g., Miyazaki et al., 2012, 2017).

Satellite measurements have been used to constrain natural NO_x sources as well, predominantly biomass burning (e.g., Mebust et al., 2011; Huijnen et al., 2012; Mebust and Cohen, 2013, 2014; Bousserez, 2014; Schreier et al., 2014; Castellanos et al., 2015; van Marle et al., 2017), lightning (e.g., Beirle et al., 2004; Martin et al., 2007; Beirle et al., 2010; Bucsela et al., 2010; Miyazaki et al., 2014; Pickering et al., 2016; Nault et al., 2017), and soil NO_x (e.g., van der A et al., 2008; Hudman et al., 2010, 2012; Zörner et al., 2016). The episodic and geographically disparate nature of these sources (especially lightning and biomass burning) make satellite observations an ideal method to constrain their emissions, given satellites' continuous data record and broad geographic coverage.

The current fleet of space-based sensors measures NO_2, not total NO_x, but due to the rapid daytime equilibrium between NO and NO_2, this allows inferences about tropospheric NO_x to be made from NO_2 measurements. For a measurement of tropospheric NO_2, several steps are required. First, a UV-visible spectrometer records geolocated solar reflectances from the Earth's surface and a reference spectrum of the sun. Then, absorbances in backscattered sunlight are fit using differential optical absorption spectroscopy (DOAS) or a similar technique to yield a total slant column density (SCD). This quantity represents the amount of NO_2 per unit area, integrated along all light paths that reach the detector (Boersma et al., 2001; Richter and Wagner, 2011). Next, the tropospheric and stratospheric NO_2 columns are separated. There are several approaches; some examples include using a data assimilation system to constrain modeled stratospheric columns (Boersma et al., 2011) and an iterative process assuming that areas known a priori to have little tropospheric NO_2 are all stratospheric NO_2 and interpolating to fill in polluted areas (Bucsela et al., 2013). Finally, the tropospheric SCD is converted into a vertical column density (VCD) in order to account for pixel-to-pixel differences in path length and sensitivity to NO_2. The conversion factor from the SCD to the more geophysically relevant and easily understood VCD is the air mass factor (AMF, Palmer et al., 2001; Burrows et al., 1999; Slusser et al., 1996; McKenzie et al., 1991).

An AMF is computed by simulating an SCD and VCD for each retrieved pixel. Typically, an a priori NO_2 profile is simulated with a chemical transport model (CTM) such as GEOS-Chem, WRF-Chem, the GMI-CTM, TM4, or TM5. The modeled VCD can be calculated by integrating this profile over the troposphere. The modeled SCD requires a radiative transfer model, such as TOMRAD, SCIATRAN, or VLIDORT, in combination with the a priori NO_2 profile in order to compute the light absorbed by NO_2 and thus the SCD that yields that absorbance. The radiative transfer calculations also require a priori inputs: the sun-satellite geometry, surface reflectance, and surface elevation are all necessary. Knowledge of the cloud and aerosol properties in the pixel is also necessary to account for their effects on light scattering in the radiative transfer calculations. Aerosol effects are often assumed to be implicitly accounted for in cloud properties (e.g., Boersma et al., 2011), but have been treated explicitly by some products (e.g., Lin et al., 2015).

The accuracy of these input data has a significant impact on the accuracy of the AMFs and therefore the vertical columns. Lorente et al. (2017) compared seven retrievals and found that input assumptions were responsible for a 42 % structural uncertainty in AMFs over polluted areas. A key concern is the resolution of the input data. CTMs are computationally expensive, requiring a trade-off between spatial and temporal resolution and domain size. For global products, model resolutions of $3° \times 2°$ (Boersma et al., 2011) to $1° \times 1°$ (Krotkov et al., 2017) are typical. Russell et al. (2011) found that increasing the resolution of the NO_2 profiles from $2.5° \times 2°$ to 4 km altered the retrieved VCDs by up to 75 %, primarily by capturing the urban–rural gradient in surface NO_2 concentrations. McLinden et al. (2014) found that increasing the a priori profiles' resolution from $3° \times 2°$ to 15 km resulted in a factor of 2 increase in NO_2 column over the Canadian oil sands. Laughner et al. (2016) examined the effect of the profiles' temporal resolution, and identified up

to 40 % changes in individual VCDs using day-to-day NO_2 profiles compared to monthly averaged profiles. The current trade-off to obtain such high-resolution profiles is that the resulting product is only available over a subset of the world, rather than globally.

The Berkeley High Resolution (BEHR) Ozone Monitoring Instrument (OMI) NO_2 retrieval is one such regional product that provides tropospheric NO_2 VCDs over part of North America (approximately 125 to 65° W, 25 to 50° N) using high-resolution a priori inputs. The BEHR product has been used in numerous studies covering areas of research such as NO_x trends (Russell et al., 2012; Kharol et al., 2015; Pusede et al., 2016; Parker et al., 2017), anthropogenic emissions (de Foy et al., 2015; Jiang et al., 2018), soil emissions (Hudman et al., 2012), land use regression modeling (Bechle et al., 2015), and model evaluation (Canty et al., 2015; Travis et al., 2016).

Here we describe the updates from v2.1C to v3.0B. (For information on v2.1C, see Russell et al., 2011, and the changelog at http://behr.cchem.berkeley.edu/Portals/2/Changelog.txt, last access: 14 November 2018.) There are seven primary changes.

1. Updated to use the v3.0 NASA tropospheric SCDs
2. Surface reflectance updated from version 5 MODIS black sky albedo to version 6 MODIS BRF product
3. New a priori NO_2 profiles, with specific changes:
   a. Lightning NO_2 included
   b. Monthly profiles use 2012 emissions, instead of 2005 emissions used in v2.1C and prior
   c. Daily profiles, with year-specific emissions, used for as many years as possible
4. Temperature profiles taken from WRF-Chem instead of the previous coarse climatology
5. A new gridding method was implemented that corrected issues with grid cells on the border between two pixels not being allocated a value
6. A variable tropopause height derived from WRF simulations replaced the previous fixed 200 hPa tropopause in the AMF calculations.
7. Surface pressure calculation was changed to follow Zhou et al. (2009) using GLOBE terrain elevation and WRF surface pressure

These changes all affect the tropospheric VCDs. BEHR also provides a "visible-only" VCD, that is, the VCD excluding NO_2 below clouds for users interested in, e.g., cloud slicing methods (Choi et al., 2014). These visible-only VCDs are computed by dividing the tropospheric slant columns by the corresponding visible-only AMF. BEHR v3.0A implemented a more physically intuitive form of the visible-only AMF than that in v2.1C. This change is described in the Supplement for interested users.

In this paper, we describe each change in detail and examine the effect of each individual change on the calculated VCDs. v3.0A was available on the BEHR website (behr.cchem.berkeley.edu, last access: 14 November 2018) between November 2017 and July 2018; v3.0B replaced v3.0A on the website and the static repositories (Laughner et al., 2018a, b, c, d) in July 2018. Therefore, in this paper, we will separate changes implemented in v3.0A from those in v3.0B, so that the differences between v3.0A and v3.0B can be accounted for if any results are published using v3.0A. Changes implemented in v3.0A are described first, followed by those implemented in v3.0B. Validation of v3.0B is described separately in Laughner et al. (2018e).

Because of the computational resources required to simulate daily a priori NO_2 profiles, BEHR v3.0B is produced for all years from 2005 on using monthly average NO_2 profiles, and for as many years as possible with daily NO_2 profiles. The latter is available for 2005–2010 and 2012–2014, with the remaining years following as the simulations of the necessary NO_2 profiles are completed. In this paper, we focus on the 2012 data as an example to understand the effect each change to the algorithm has on the final VCDs.

2 Methods: BEHR

Unless otherwise noted, the following methods description applies to both BEHR versions 3.0A and 3.0B. A summary of the differences in methods between v3.0A and v3.0B is listed in Table 2.

2.1 NO_2 VCD calculation

The BEHR product calculates tropospheric vertical column densities (VCDs) starting from the tropospheric slant column densities (SCDs) from the NASA Standard Product, v3.0 (Krotkov et al., 2017; Krotkov and Veefkind, 2016), by

$$V_{\mathrm{BEHR}} = \frac{S_{\mathrm{NASA}}}{A_{\mathrm{BEHR}}}, \tag{1}$$

where V_{BEHR} and S_{NASA} are the BEHR VCD and NASA SCD, respectively, and A_{BEHR} is a custom tropospheric air mass factor (AMF), computed with

$$A_{\mathrm{BEHR}} = \frac{(1-f)\int_{p_{\mathrm{surf}}}^{p_{\mathrm{trop}}} w_{\mathrm{clear}}(p) g(p)\,\mathrm{d}p + f\int_{p_{\mathrm{cloud}}}^{p_{\mathrm{trop}}} w_{\mathrm{cloudy}}(p) g(p)\,\mathrm{d}p}{\int_{p_{\mathrm{surf}}}^{p_{\mathrm{trop}}} g(p)\,\mathrm{d}p} \tag{2}$$

where f is the cloud radiance fraction, and w_{clear} and w_{cloudy} are the scattering weights for clear and cloudy subscenes (i.e., parts of the pixel), respectively, p_{trop} is the tropopause

pressure, p_{surf} is the ground surface pressure, p_{cloud} is the cloud optical centroid pressure, and $g(p)$ is the NO_2 a priori profile in mixing ratio (Sect. 2.6). The calculation of both p_{surf} and p_{trop} differ between v3.0A and v3.0B; see Sects. 2.3 and 2.4, respectively.

This method produces VCDs that include an estimated below-cloud component, and thus can be considered a total tropospheric column. This is desirable for applications focusing on near-surface NO_2, and are stored in the BEHR data as "BEHRColumnAmountNO2Trop". Other applications (e.g., cloud slicing) benefit from having a "visible-only" tropospheric AMF that only retrieves NO_2 above the cloud in a cloudy subscene. For these "visible-only" AMFs, Eq. (2) is replaced with

$$A_{\mathrm{BEHR,vis}} = \frac{(1-f)\int_{p_{surf}}^{p_{trop}} w_{clear}(p)g(p)\,\mathrm{d}p + f\int_{p_{cloud}}^{p_{trop}} w_{cloudy}(p)g(p)\,\mathrm{d}p}{(1-f_g)\int_{p_{surf}}^{p_{trop}} g(p)\,\mathrm{d}p + f_g\int_{p_{cloud}}^{p_{trop}} g(p)\,\mathrm{d}p}, \quad (3)$$

where f_g is the geometric cloud fraction. The numerator is the same as in Eq. (2), in both cases representing a modeled slant column density. The denominator in Eq. (2) is the total modeled tropospheric column, while in Eq. (3) it is only the visible modeled column. Replacing A_{BEHR} in Eq. (1) with $A_{\mathrm{BEHR,vis}}$ yields a visible-only NO_2 column as the output, stored in the variable "BEHRColumnAmountNO2TropVisOnly" in the BEHR files. The form of this visible AMF changed from v2.1C to v3.0A; please see Sect. S1 in the Supplement for details of the old calculation.

The scattering weights (w_{clear} and w_{cloudy}) are computed from the same look-up table (LUT) as the NASA SP v2.1 and v3.0 (Bucsela et al., 2013; Krotkov et al., 2017). The scattering weights depend on the solar zenith angle (SZA, θ_S), viewing zenith angle (VZA, θ_V), relative azimuth angle (RAA, ϕ_R), surface reflectance (Sect. 2.2), and surface pressure (Sect. 2.3). A vector of scattering weights is looked up using 5-D multilinear interpolation to obtain the scattering weights for the above input parameters. Note that the RAA is calculated as

$$\phi_{R,\,tmp} = \left|180 + \phi_S - \phi_V\right|, \quad (4)$$

$$\phi_R = \begin{cases} \phi_{R,\,tmp} & \text{if} \quad \phi_{R,\,tmp} \in [0, 180], \\ 360 - \phi_{R,\,tmp} & \text{if} \quad \phi_{R,\,tmp} > 180, \end{cases} \quad (5)$$

where ϕ_S and ϕ_V are the solar and viewing azimuth angles, respectively, defined in degrees, and $\phi_{R,\,tmp}$ is a temporary variable. The extra factor of 180 in Eq. (4) accounts for the RAA definition used in the scattering weight look-up table (where $\phi_R = 0$ indicates that the satellite is opposite the sun, i.e., in the forward scattering position), while Eq. (5) ensures that ϕ_R is between 0 and 180°.

A temperature correction, $\alpha(p)$ (Bucsela et al., 2006, 2013), is applied to the scattering weights interpolated from the look-up table, such that $w(p)$ in Eqs. (2) and (3) is equal to $\alpha(p)w_0(p)$, where $w_0(p)$ is the pressure-dependent scattering weights from the look-up table and $\alpha(p)$ is

$$\alpha(p) = 1 - 0.003 \cdot (T(p) - 220), \quad (6)$$

$$\alpha(p) \in [0.1, 10], \quad (7)$$

where Eq. (7) indicates that $\alpha(p)$ is constrained to the range 0.1 to 10. $T(p)$ is a temperature profile taken from the same WRF-Chem simulation as the NO_2 a priori profiles (Sect. 2.6).

2.2 Surface reflectivity

2.2.1 Over land

BEHR v3.0 uses a bidirectional reflectance factor (BRF) to represent surface reflectivity over land. The BRF is given by Stahler et al. (1999) as

$$R(\theta_S, \theta_V, \phi_R, \Lambda) = f_{iso}(\Lambda) + f_{vol}(\Lambda)K_{vol}(\theta_S, \theta_V, \phi_R) + f_{geo}(\Lambda)K_{geo}(\theta_S, \theta_V, \phi_R), \quad (8)$$

where R is the surface reflectivity, f_{iso}, f_{vol}, and f_{geo} are coefficients representing the relative contributions of different types of scattering, and K_{vol} and K_{geo} are kernels representing the directional dependence of the reflectivity. Λ represents a wavelength band, which here is band 3 of the MODIS instrument (459–479 nm).

K_{vol} is the RossThick kernel (Roujean et al., 1992) and K_{geo} is the LiSparse kernel (Wanner et al., 1995), corrected to be reciprocal in θ_S and θ_V. BEHR calculates both kernels using the formulations given in Stahler et al. (1999). The coefficients, f_{iso}, f_{vol}, and f_{geo}, are taken at 30 arcsec resolution from the MODIS MCD43D07 (Schaaf, 2015a), MCD43D08 (Schaaf, 2015b), and MCD43D09 (Schaaf, 2015c) BRF products, respectively. Quality information for these coefficients is obtained from the MCD43D31 product (Schaaf, 2015d). (The combination of these four products will henceforth be referred to as MCD43Dxx.) These products represent a 16-day average; in version 006 (used here), the file date is in the middle of that 16-day averaging window. BEHR uses the file dated for the day being retrieved for the BRF coefficients; i.e., for 1 June 2012, the MODIS files with 1 June 2012 in the file name are used. This means that the surface reflectivity used in BEHR incorporates land data from 8 days before and after the OMI observation.

An average surface reflectance for a given OMI pixel is calculated by computing R for each set of MCD43Dxx coefficients within the bounds of the pixel given by the FoV75 corners from the OMPIXCOR product (Kurosu and Celarier, 2010) and using the SZA, VZA, and RAA of the pixel as inputs to the kernels. All values of R from MCD43Dxx coefficients with non-fill quality flags are averaged to produce the overall surface reflectance for the pixel; however, since coefficients with quality 3 are significantly lower quality than

quality 0 to 2, if the average quality of all MCD43Dxx coefficients within the OMI pixel is ≥ 2.5, the pixel is flagged as low quality. The pixel is also flagged if $\geq 50\,\%$ of the MCD43Dxx coefficients have a fill value for the quality (see Sect. A3).

2.2.2 Over water

The MCD43Dxx products do not contain coefficients over deep water; therefore, an alternate measure of surface reflectance is needed. We use the University of Maryland land map (ftp://rsftp.eeos.umb.edu/data02/Gapfilled/Land_Water_Mask_7Classes_UMD.hdf, last access: 28 November 2017) to classify OMI pixels as land or water. Land classes 0 (shallow ocean), 6 (moderate or continental ocean), and 7 (deep ocean) are considered ocean; all others are considered land. The mask is given at 30 arcsec resolution; if $> 50\,\%$ of the mask data points within the FoV75 bounds of the OMI pixel are ocean, the pixel is treated with an ocean surface reflectance.

Ocean surface reflectance is parameterized by SZA using output from the Coupled Ocean Atmosphere Radiative Transfer (COART) model (Jin et al., 2006, hosted at https://satcorps.larc.nasa.gov/jin/coart.html, last access: 2 March 2018). The ratio of upwelling to downwelling radiation was simulated for 18 solar zenith angles (0 to 85° at 5° increments). Additional settings are given in Table 1. The ratio of upwelling to downwelling radiation is linearly interpolated to the SZA of the OMI pixel, and that interpolated ratio is taken as the surface reflectance of the ocean pixel. In v3.0A, COART-simulated reflectance at 430 nm was used; in v3.0B, reflectance at 460 nm was used.

2.3 Surface pressure

The surface elevation of each OMI pixel is computed by averaging all surface elevation values from the Global Land One-kilometer Base Elevation (GLOBE) database (Hastings and Dunbar, 1999) within the FoV75 bounds of the pixel. From v3.0B on, pixel surface pressure is calculated using the method recommended by Zhou et al. (2009):

$$p = p_{\mathrm{WRF}}\left(\frac{T_{\mathrm{WRF}}}{T_{\mathrm{WRF}} + \Gamma \cdot (h_{\mathrm{WRF}} - h_{\mathrm{GLOBE}})}\right)^{-g/\mathrm{R}\Gamma}, \quad (9)$$

where p is the pixel surface pressure, p_{WRF}, T_{WRF}, and h_{WRF} are the surface pressure, temperature, and elevation from the WRF model, h_{GLOBE} is the averaged GLOBE surface elevation, g is gravitational acceleration ($9.8\,\mathrm{m\,s^{-2}}$), R is the gas constant for dry air ($287\,\mathrm{J\,kg^{-1}\,K^{-1}}$) and Γ the lapse rate ($0.0065\,\mathrm{K\,m^{-1}}$).

Prior to v3.0B, the surface pressure was computed by converting the average GLOBE surface elevation to a pressure using a fixed scale height calculation:

$$p = (1013.25\ \mathrm{hPa})e^{-z/7400\ \mathrm{m}}, \quad (10)$$

Table 1. Additional settings for the COART model used to simulate ocean reflectivity. "Atmospheric profile" refers to the distribution of total precipitable water, O_3, CO_2, and CH_4.

Wavelength	430 nm (v3.0A), 460 nm (v3.0B)
Atmospheric profile	Mid-latitude summer
Boundary layer aerosol model	MODTRAN maritime
Stratospheric aerosol model	Background stratosphere
Total aerosol loading	AOD at 500 nm = 1
Wind speed	$5\,\mathrm{m\,s^{-1}}$
Ocean depth	100 m
Chlorophyll	$0.2\,\mathrm{mg\,m^{-3}}$
Ocean particle scattering	Petzold average, $bb/b = 0.0183$
Bottom surface albedo	0.1

where z is the average surface elevation in meters.

2.4 Tropopause pressure

For the upper integration limit in Eq. (2), BEHR v3.0A and prior versions used a fixed tropopause pressure (200 hPa). BEHR v3.0B utilizes a thermal tropopause pressure derived from temperature profiles from the same WRF-Chem simulation as the NO_2 a priori profiles. The thermal tropopause is defined as the lowest level at which the average lapse rate between this level and all higher levels within 2 km does not exceed $2\,\mathrm{K\,km^{-1}}$ by World Meteorological Organization (1957). The calculation operationally works in most regions; however, occasionally a discontinuity occurs between adjacent pixels where both pixels approach the $2\,\mathrm{K\,km^{-1}}$ threshold at the same model level but only one exceeds the threshold at that level. As this discontinuity is only due to the choice of the standard threshold for lapse rate in the criteria, an additional filtering is implemented to identify pixels with abrupt transition in calculated tropopause pressure. New tropopause pressures for these pixels are derived by linear interpolation of tropopause pressures from the nearest valid pixels after filtering.

2.5 Cloud products

BEHR contains several cloud fraction products: a geometric cloud fraction derived from the O_2–O_2 algorithm (Acarreta et al., 2004), a cloud radiance fraction calculated by NASA from the O_2–O_2 product, and a geometric cloud fraction derived from the Aqua MODIS instrument (which currently makes observations ~ 8 min before OMI). Additionally, cloud pressure from the OMI O_2–O_2 algorithm (Acarreta et al., 2004) is included. The OMI-derived quantities are the same as those in the NASA SP v3.0. The MODIS cloud product used is MYD06_L2 (Platnick et al., 2015).

Russell et al. (2011) found that the MODIS cloud product was less likely to give erroneously large cloud fractions due to high surface reflectivity over the California and Nevada desert, and concluded that this more than offset any error

Table 2. Summary of differences in methods between v3.0A and v3.0B.

Component	v3.0A	v3.0B	Section
Ocean reflectance	Calc. for 430 nm	Calc. for 460 nm	2.2
Surface pressure	Scale height	WRF pressure adjusted with GLOBE elevation	2.3
Tropopause pressure	Fixed at 200 hPa	Calculated from WRF temperature profiles	2.4
Daily prof. hour	Last hour before overpass	Closest hour to overpass	2.6.2

caused by the small separation between the overpass times (currently ~ 8 min) of OMI onboard the Aura satellite and MODIS onboard the Aqua satellite. We continue to provide the MODIS cloud product for cloud filtering; however, because it does not cover the full OMI swath, we use the OMI cloud fractions in the AMF calculations.

As with the MODIS BRF product, all values of cloud fraction given in MYD06_L2 within each OMI pixel's bounds defined by the FoV75 pixel corners are averaged to yield the MODIS-derived cloud fraction for that OMI pixel. Unlike the BRF product, only Level 2 MODIS granules with times between the start and end times of the current OMI orbit are used.

2.6 A priori profiles

From v3.0A onward, BEHR is divided into two subproducts which differ in the temporal resolution of the a priori NO_2 profiles. Based on the results in Laughner et al. (2016), using a priori profiles specifically simulated for each day of BEHR observations is preferable; however, the computational cost of doing so limits the time periods that such profiles can be simulated for. Therefore a second subproduct using monthly average profiles derived from the 2012 a priori profiles is available that covers all years of the OMI data record. This assumes that monthly average profiles are applicable to years other than that for which they were simulated; while not a perfect assumption, it has successfully been used in previous NO_2 products (e.g., Bucsela et al., 2013).

In this section, we describe the model configuration used to generate the a priori profiles. General model settings will be described first, followed by information specific to the implementation of daily and monthly average profiles in the BEHR algorithm.

2.6.1 WRF-Chem configuration

NO_2 and temperature a priori profiles are generated using version 3.5.1 of WRF-Chem (Grell et al., 2005) run at 12 km resolution across the continental United States (Fig. S6 in the Supplement). The North American Regional Reanalysis (NARR) dataset is used to drive the meteorological initial and boundary conditions, as well as four-dimensional data analysis (FDDA) nudging (Liu et al., 2006). U and V winds, temperature, and water vapor are nudged at all levels with nudging coefficients of $0.0003\ s^{-1}$.

Anthropogenic emissions are driven by the National Emissions Inventory 2011 (NEI 11) gridded to 12 km resolution. Each year's emissions are scaled by the ratio of that year's total annual emissions to 2011 emission. These total emissions are provided by the Environmental Protection Agency (EPA, 2016). Biogenic emissions are driven by the Model of Emissions of Gases and Aerosols from Nature (MEGAN, Guenther et al., 2006). Lightning emissions are driven by the recommended settings in Laughner and Cohen (2017) for a simulation using FDDA nudging.

Chemistry in WRF-Chem is simulated using the RACM2_Berkeley2 mechanism (Zare et al., 2018), which is based on the Regional Atmospheric Chemistry Mechanism, version 2 (RACM2, Goliff et al., 2013) with updates to alkyl nitrate and nighttime chemistry (Browne et al., 2014; Schwantes et al., 2015) and the inclusion of methylperoxy nitrate (MPN) chemistry (Browne et al., 2011; Nault et al., 2015, 2016).

Chemical boundary conditions for WRF-Chem are taken from two different global models. For model years 2007 and later, chemical concentrations from the Model for Ozone and Related chemical Tracers (MOZART, Emmons et al., 2010) provided by the National Center for Atmospheric Research (NCAR) at https://www.acom.ucar.edu/wrf-chem/mozart.shtml (last access: 14 November 2018) are used, converted to boundary conditions for WRF-Chem using the MOZBC utility. MOZART data are not available from NCAR for years prior to 2007; instead, the chemical data are taken from GEOS-Chem model v9-02 (at $2.5° \times 2.0°$ resolution), with updates from Nault et al. (2017). These updates are detailed in Sect. S3. GEOS-Chem instantaneous output is sampled every 3 h. This output is transformed into netCDF files for input into the MOZBC utility by use of the gc2moz utility of the AutoWRFChem package (Laughner, 2017).

Each year is simulated with a 1-month spinup at the anthropogenic emissions levels for that year. The year is simulated continuously, without reinitialization. Instantaneous WRF-Chem output is sampled hourly. For 2007, since MOZBC data were not available for December 2006, boundary conditions for 1 January 2007 were repeated for the first 32 days of the simulation (1 December 2006 to 1 January 2007) to allow the model time to spin up from the initial conditions.

In the BEHR AMF calculation, the profiles are interpolated to the same pressures that the scattering weights are

defined on. The NO_2 mixing ratio profiles are interpolated in log–log space (e.g., $\ln(NO_2)$ given at $\ln(p_{WRF})$ is interpolated to $\ln(p_{BEHR})$, Bucsela et al., 2008). Temperature is interpolated in semilog space (T given at $\ln(p_{WRF})$ is interpolated to $\ln(p_{BEHR})$, since lapse rates assume a linear relationship between temperature and altitude, and altitude is proportional to $\ln(p)$. The profiles are also extrapolated to one scattering weight pressure level above and below the top and bottom of the WRF profile, respectively. This accounts for the possibility that, e.g., a pixel's surface pressure may be slightly below the WRF surface pressure, but limiting the extrapolation to only one level should minimize errors due to extrapolation. Once interpolated and extrapolated, all profiles within the FoV75 bounds of the OMI pixel are averaged to give the profiles used in calculating the AMF.

2.6.2 Daily a priori profiles

We make use of daily profiles for as much of the OMI data record as it is computationally feasible to simulate these profiles. Both NO_2 a priori profiles and the temperature profiles necessary for the scattering weight temperature correction are drawn from the same simulation. WRF-Chem is configured to provide instantaneous output at the top of every hour. In v3.0A, the last WRF-Chem profile before the average time of the OMI pixels over the domain is chosen to provide the a priori NO_2 and temperature profiles. In v3.0B, the profile closest in time to the average OMI time is used. These profiles are binned to OMI pixels as described in Sect. 2.6.1.

As of this writing, daily profiles have been simulated for 2005 to 2010 and 2012 to 2014. Profiles for 2011 are in progress, and profiles for 2015 and later years will be simulated as time and computational resources permit.

2.6.3 Monthly a priori profiles

Given the computational cost in producing daily a priori profiles, we continue to use monthly average profiles as well to cover years for which daily a priori profiles have not yet been simulated. Monthly profiles are generated from 2012 WRF-Chem output. As in Laughner et al. (2016), an average of all available hourly profiles for a given month weighted by weights w_l is given by

$$w_l = 1 - |13.5 - (l/15) - h|,$$
$$w_l \in [0, 1], \tag{11}$$

where l is the profile longitude and h is the UTC hour of the profile. This formulation gives highest weight to profiles near OMI overpass time (approximately 13:30 local standard time) while smoothly interpolating between adjoining time zones. The appropriate month's profiles are spatially matched to OMI pixels in the same manner as the daily profiles (Sect. 2.6.2).

3 Paper structure

In Sects. 4 and 5, we evaluate the effect each change to the BEHR algorithm between v2.1C and v3.0B had on the tropospheric VCDs. In order to provide a clear history, changes introduced in v3.0A will be discussed first (Sect. 4), followed by changes introduced in v3.0B (Sect. 5). V3.0A incorporated all changes up through the introduction of the new gridding algorithm; the remainder are added in v3.0B. Changes to the visible-only VCDs (i.e., those excluding the below-cloud column) are discussed in the Supplement (Sect. S1). Following this the overall difference between v2.1C and v3.0B will be presented in Sect. 6. Recommendations for the use of the product are given in Sect. 7. A description of the data format is given in Appendix A.

For the discussion of how changes to the algorithm affect the NO_2 VCDs, Figs. 1 and 2 and Tables 3 and 4 are the central focus. Each panel shows the change in the BEHR NO_2 VCDs resulting from a specific change to the algorithm. To generate these figures, BEHR VCDs were computed after adding each change to the algorithm incrementally. Each panel in the figures and line in the tables shows the percent change in VCDs due to the corresponding change to the algorithm. These are computed relative to VCDs with one fewer change to the algorithm; for example, Fig. 1b is the percent difference between VCDs using the new NASA SCDs and the new MODIS BRF surface reflectance versus VCDs using just the new NASA SCDs. Figures 1a and 2a and the first lines in Tables 3 and 4 are relative to BEHR v2.1C.

Figure 1 shows the percent change of average BEHR tropospheric VCDs due to each algorithm improvement for the subproduct using monthly average NO_2 a priori profiles, while Fig. 2 shows the changes to the subproduct using daily NO_2 a priori profiles. (Figure 2 has fewer panels than Fig. 1 as daily profiles were only possible in increments after the change to the algorithm to introduce the new a priori profiles was implemented.) Both figures are for summer (June–August) 2012. Winter changes are presented in the Supplement.

Table 3 gives the mean and median changes for each incremental improvement shown in Figs. 1 and 2; that is, it gives the domain-wide mean and median values of the time-averaged changes shown in the figures. Table 4 is similar, but is the statistics for individual pixels, rather than the time-averaged changes.

4 Changes in BEHR v3.0A

4.1 NASA v3.0 slant columns

Version 3.0 of the NASA Standard Product introduced a new method of fitting the observed Earthshine radiances to yield total SCDs (Krotkov et al., 2017; Marchenko et al., 2015). This new fitting approach eliminates a positive bias identified by Belmonte Rivas et al. (2014), and reduces the total SCDs

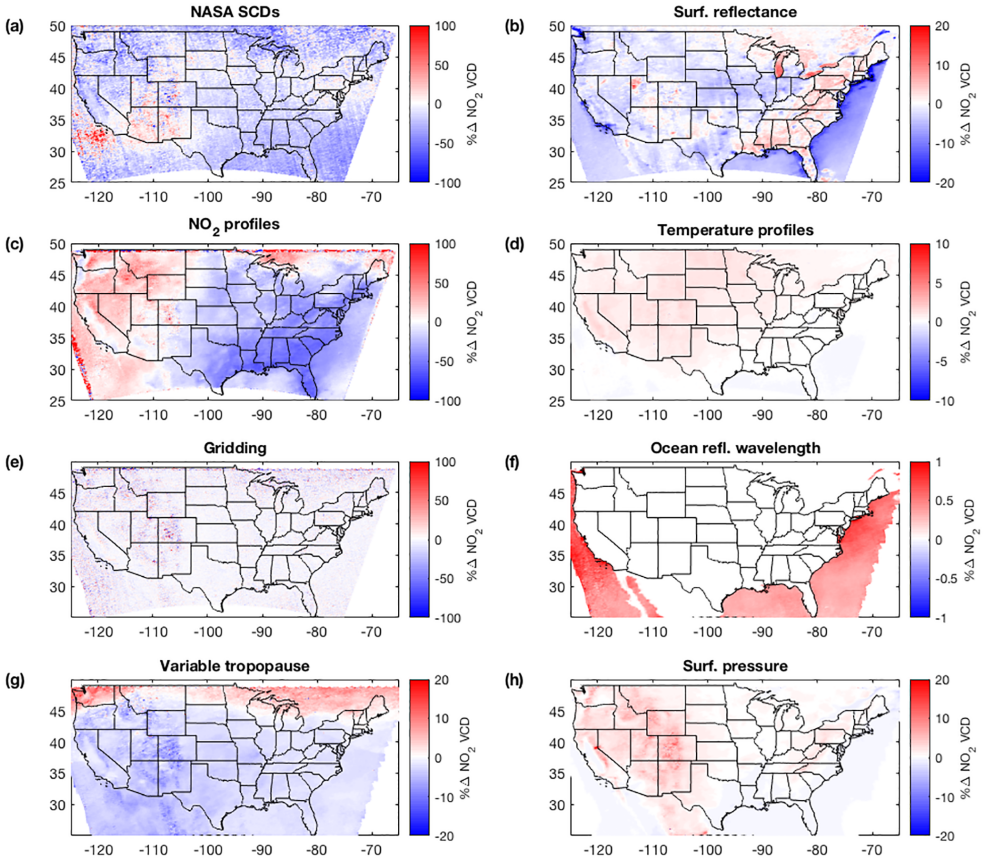

Figure 1. Percent change in the tropospheric NO_2 column due to each of the algorithm improvements. Changes due to **(a)** new NASA SCDs, **(b)** new surface reflectance, **(c)** new monthly NO_2 profiles, **(d)** new temperature profiles, **(e)** new gridding method, **(f)** change in ocean reflectance LUT from 430 to 460 nm, **(g)** switch to WRF-derived tropopause pressure, **(h)** switch to Zhou et al. (2009) surface pressure methodology. Note that the color scale varies among the plots. Averages are for June–August 2012 and exclude pixels affected by the row anomaly and with cloud fraction > 0.2. Monthly average a priori profiles are used for all differences. Wintertime changes and histograms are given in Sect. S5.

retrieved. For much of the globe, this reduction is attributed to the stratospheric SCD, but over the continental US, it is attributed to the tropospheric SCD. Thus, the broad reduction in tropospheric VCDs seen here (Fig. 1a, Tables 3 and 4) due to the new SCD fitting is consistent with Krotkov et al. (2017).

4.2 Surface reflectance

4.2.1 Land reflectance

BEHR v3.0A calculated the land surface reflectance by using the BRF coefficients computed from the MODIS instruments to compute the directional surface reflectance for the solar and viewing angles specific to each pixel. Previous versions of BEHR used a black-sky albedo with no directional dependence. The version of the MODIS surface reflectance products used was also upgraded from version 5 in BEHR v2.1C and prior to version 6 in BEHR v3.0A.

Figure 1b shows the difference in summertime NO_2 VCDs resulting from the change in surface reflectance products. Figure 3, panels a and d, show the overall summer and winter changes in surface reflectance. Panels b, c, e, and f decompose this change into the change in the MODIS product version (version 5 to 6, panels b and e) and from black sky to BRF (panels c and f).

Generally, UV-vis AMFs increase (thus NO_2 VCDs decrease) with increasing surface reflectance, due to greater sensitivity to near surface NO_2. This pattern is apparent when comparing Figs. 1b and 3a, as changes in the NO_2 VCDs show the expected inverse relationship to the changes in surface reflectance. These changes in average surface reflectance are due primarily to the upgrade from version 5 to version 6 of the MODIS product, as we see larger average changes in land surface reflectance between the version 5 and 6 black-sky product (Fig. 3b, e) than between the version 6 black-sky and BRF products (Fig. 3c, f). Further, we see that the spatial pattern due to the surface reflectance seen in

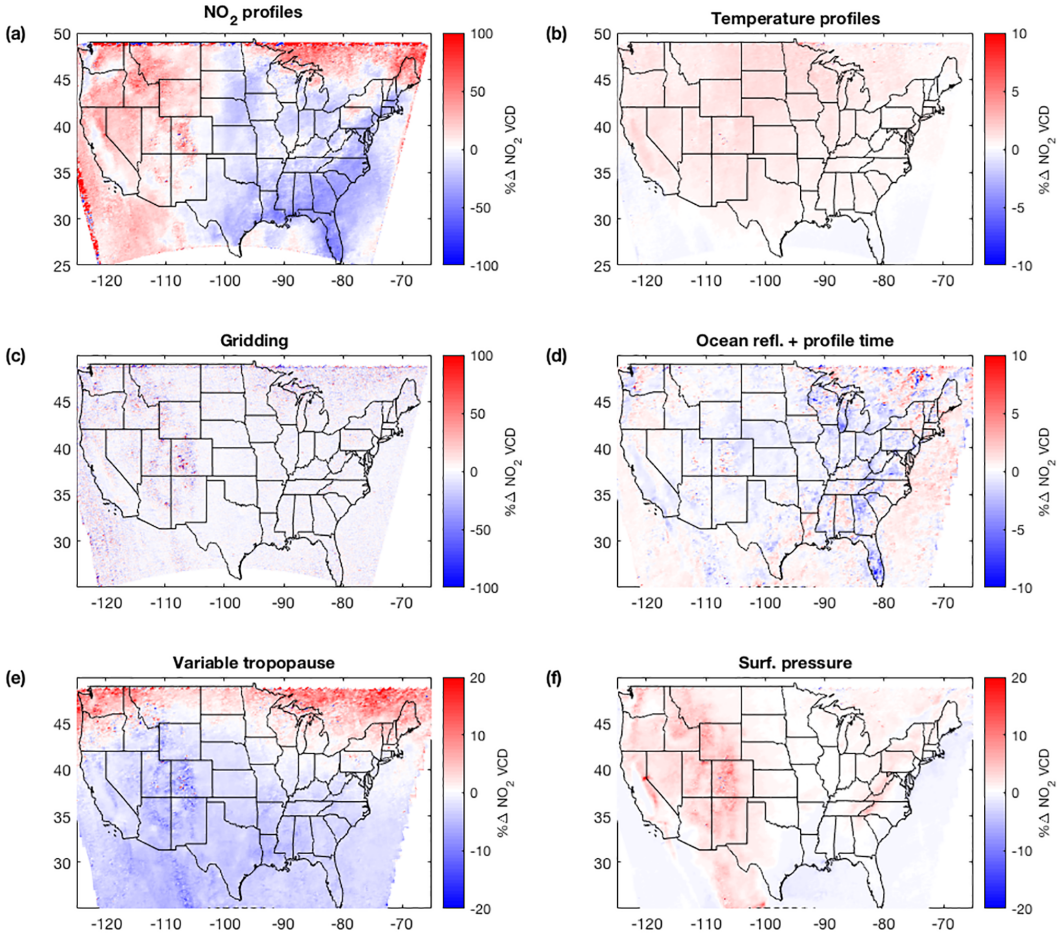

Figure 2. Percent change in the total tropospheric NO_2 column due to each of the algorithm improvements for the subproduct using daily profiles. Changes due to **(a)** new NO_2 profiles, **(b)** new temperature profiles, **(c)** new gridding, **(d)** change in profile time selection and ocean reflectance LUT from 430 to 460 nm, **(e)** switch to WRF-derived tropopause pressure, **(f)** switch to the Zhou et al. (2009) surface pressure methodology. Note that in **(a)**, the difference is against an increment using monthly average profiles; also note that the color scale varies among the plots. Averages are for June–August 2012 and exclude pixels affected by the row anomaly and with cloud fraction > 0.2. Wintertime changes and histograms are given in Sect. S5.

the BEHR VCDs (Fig. 1b) is well correlated with the spatial pattern of changes between versions 5 and 6 of the MODIS black-sky product (Fig. 3b). Differences between versions 5 and 6 were listed at https://lpdaac.usgs.gov/dataset_discovery/modis/modis_products_table/mcd43c3_v006 (last access: 14 November 2018) as of 5 February 2018. Two improvements of note are the following.

- Change from a land cover-based backup database to one based on full inversions. Notably, the summertime decreases in surface reflectance along the east coast (Fig. 3a, b) are somewhat spatially correlated with deciduous broadleaf forest, mixed forest, and woody savanna land cover types that are rare elsewhere in the country (Fig. S8).
- Change from using the majority snow or no-snow status from the 16-day observation window to the current-day status. In Fig. 3, panels d and e, the largest changes are seen sporadically in the northern half of the country, which suggests snow cover is impacting the surface reflectance.

We have not rigorously tested these specific changes as the cause for the spatial pattern of changes in surface reflectance; rather, our point is that the change from version 5 to 6 of the MODIS products is a larger driver of the change in average surface reflectance than the change from black-sky to BRF. However, when we consider the changes of individual pixels, we find that the difference between the the black sky and BRF surface reflectance is much more variable (Fig. S7). The switch to a BRF surface reflectance is expected to improve retrieval accuracy of individual pixels and therefore is valuable to users interested in day-to-day variations in NO_2 VCDs (Vasilkov et al., 2017).

Table 3. Percent differences in averaged NO_2 VCDs for each increment. Means are given with 1σ uncertainties; medians are given with uncertainties as the distance to the upper and lower quartiles. "Monthly" and "Daily" in the first column indicate which subproduct is considered (Sect. 2.6). "Ocean LUT" refers to the ocean surface reflectance LUT. Outliers were removed before calculating these statistics.

		JJA		DJF	
		Mean	Median	Mean	Median
Monthly	SCDs	-14 ± 14	-13^{+9}_{-9}	-21 ± 15	-21^{+9}_{-9}
	Surf. refl.	-1.5 ± 2.8	$-1.4^{+1.8}_{-1.8}$	0.2 ± 6.9	$0.2^{+3.6}_{-4.3}$
	NO_2 profiles	-9.8 ± 24.3	-11^{+20}_{-16}	-0.5 ± 7.7	$0.3^{+3.3}_{-4.2}$
	Temperature profiles	0.5 ± 0.4	$0.4^{+0.4}_{-0.3}$	1.5 ± 0.9	$1.4^{+0.8}_{-0.7}$
	Gridding	-0.7 ± 6.6	$-0.6^{+4.0}_{-4.0}$	-0.6 ± 10.5	$-0.6^{+6.3}_{-6.2}$
	Ocean LUT/profile time*	0.4 ± 0.1	$0.4^{+0.1}_{-0.05}$	0.4 ± 0.2	$0.4^{+0.1}_{-0.1}$
	Variable trop.	-2.4 ± 1.5	$-2.2^{+0.6}_{-1.0}$	1.9 ± 2.4	2^{+1}_{-1}
	Hypsometric surf. pres.	0.5 ± 0.9	$0.3^{+0.7}_{-0.4}$	0.7 ± 0.9	$0.4^{+0.7}_{-0.4}$
Daily	NO_2 profiles	0.9 ± 20.1	$-0.5^{+15.5}_{-12.3}$	-1.3 ± 10.0	$-0.03^{+4.69}_{-6.72}$
	Temperature profiles	0.6 ± 0.5	$0.6^{+0.3}_{-0.4}$	1.5 ± 1.2	$1.2^{+1.0}_{-0.6}$
	Gridding	-0.8 ± 6.8	$-0.8^{+4.1}_{-4.1}$	-0.6 ± 10.6	$-0.7^{+6.4}_{-6.2}$
	Ocean LUT/profile time	0.04 ± 0.67	$0.04^{+0.40}_{-0.41}$	-0.08 ± 0.56	$-0.04^{+0.28}_{-0.37}$
	Variable trop.	-1.9 ± 2.4	$-2.3^{+1.6}_{-1.2}$	2.6 ± 2.6	$2.3^{+1.8}_{-1.2}$
	Hypsometric surf. pres.	0.6 ± 1.0	$0.4^{+0.9}_{-0.4}$	1 ± 1	$0.6^{+1.2}_{-0.6}$

* Statistics only for ocean pixels.

4.2.2 Ocean reflectance

BEHR v2.1C used an ocean reflectance look-up table embedded in the core code that defined the dependence of the ocean reflectance on solar zenith angle (SZA). As documentation of the source of this table is not available, BEHR v3.0A switched to a new look-up table calculated explicitly using the Coupled Ocean-Atmosphere Radiative Transfer (COART) model (Jin et al., 2006). The difference in the SZA dependence of the look-up tables is shown in Fig. 3g. The overall shape is similar, but the difference between small and large SZAs is less pronounced in the new ocean look-up table. Both are similar to the ocean surface reflectance calculated by Jin et al. (2004) for an atmospheric aerosol optical depth of 1, but for different wind speeds: the BEHR v2.1C look-up table is more characteristic of slow ($< 1\,m\,s^{-1}$) winds, while the v3.0A table assumes a wind speed of $5\,m\,s^{-1}$.

At small SZAs characteristic of summer OMI observations ($< 35°$), the new look-up table yields a $\sim 50\,\%$ greater ocean reflectance than the old table, which leads to the off-shore reflectance changes seen in Fig. 3a. At larger SZAs more characteristic of winter (~ 40 to $60°$), the difference between the old and new look-up tables shrinks, resulting in less change in the wintertime ocean surface reflectance (Fig. 3d).

Especially in summer, since the relative change in the ocean surface reflectance is large, using the new ocean look-up table does result in large relative changes to the NO_2 VCDs. Along the coasts, these changes can reach 2×10^{15} to 3×10^{15} molec. cm^{-2} (or more near New York, NY), but away from the coasts, the absolute differences are quite small.

4.3 New WRF-Chem profiles

4.3.1 Update to new monthly average profiles

There are three significant changes from the old monthly average profiles used in v2.1C and before to those used in v3.0A.

1. Lightning NO_x emissions are included in the profiles; these were not available in WRF-Chem when the previous profiles were simulated.

2. The anthropogenic emissions used now are from the National Emissions Inventory (NEI, 2011), scaled based

Table 4. Percent differences in individual pixels' NO_2 VCDs for each increment. Means are given with 1σ uncertainties; medians are given with uncertainties as the distance to the upper and lower quartiles. "Monthly" and "Daily" in the first column indicate which subproduct is considered (Sect. 2.6). "Ocean LUT" refers to the ocean surface reflectance LUT. Outliers were removed before calculating these statistics.

		JJA		DJF	
		Mean	Median	Mean	Median
Monthly	SCDs	-15 ± 49	-16^{+27}_{-27}	-21 ± 48	-20^{+24}_{-28}
	Surf. refl.	-1.6 ± 4.7	$-1.3^{+2.8}_{-3.4}$	-0.3 ± 8.6	$0.2^{+5.2}_{-6.1}$
	NO_2 profiles	-8.3 ± 25.7	$-6.9^{+15.8}_{-19.9}$	-2.1 ± 8.5	$-0.9^{+3.6}_{-5.7}$
	Temperature profiles	0.5 ± 0.5	$0.4^{+0.4}_{-0.3}$	1.2 ± 1.3	1^{+1}_{-1}
	Gridding	n/a	n/a	n/a	n/a
	Ocean LUT/profile time*	0.4 ± 0.1	$0.4^{+0.1}_{-0.1}$	0.4 ± 0.3	$0.5^{+0.2}_{-0.2}$
	Variable trop.	-2.2 ± 1.8	$-2.1^{+0.9}_{-1.2}$	1.5 ± 2.8	$1.6^{+1.6}_{-1.5}$
	Hypsometric surf. pres.	0.5 ± 0.8	$0.3^{+0.7}_{-0.3}$	0.7 ± 0.9	$0.3^{+0.9}_{-0.3}$
Daily	NO_2 profiles	1 ± 25	$2.3^{+13.7}_{-15.2}$	-2.7 ± 12.5	$-1.4^{+6.2}_{-8.8}$
	Temperature profiles	0.5 ± 0.9	$0.4^{+0.7}_{-0.5}$	1.1 ± 1.7	$0.9^{+1.3}_{-1.0}$
	Gridding	n/a	n/a	n/a	n/a
	Ocean LUT/profile time	0.1 ± 0.6	0^{+0}_{-0}	0.05 ± 0.57	0^{+0}_{-0}
	Variable trop.	-1.9 ± 2.9	$-1.8^{+1.5}_{-1.8}$	2.1 ± 3.7	$1.7^{+2.6}_{-1.6}$
	Hypsometric surf. pres.	0.5 ± 0.9	$0.2^{+0.9}_{-0.2}$	0.5 ± 0.9	$0.08^{+0.89}_{-0.08}$

* Statistics only for ocean pixels. n/a: not applicable.

on total annual emission to 2012 levels. 2012 boundary conditions and meteorology are also used. In v2.1C and earlier, NEI 2005 emissions were used.

3. The chemical mechanism was updated from the Regional Acid Deposition Model, version 2 to the custom mechanism described in Sect. 2.6.1.

The changes in the summer average VCDs due to the update to the monthly profiles are shown in Fig. 1c. The effect of including lightning NO_x emissions is most apparent, causing the $\sim 30\,\%$ decrease (5th/95th percentiles: 8 % and 55 %) in VCDs in the southeastern US (averaged east of 95° and south of 45°). This is due to the increased contribution of upper tropospheric (UT) NO_2 to the a priori profiles compared to the v2.1C profiles. As this NO_2 is located at higher sensitivity altitudes, the AMF is increased (and the retrieved VCD decreased) to reflect that higher sensitivity.

The increased VCDs along the western coast are caused by changes to the UT NO_2 profiles. The UT NO_2 over the west decreased compared to the old a priori profiles. This may be due either to the change in chemical mechanism or to a change in the O_3 boundary condition, which would affect the simulated UT $NO:NO_2$ ratio.

4.3.2 Daily vs. monthly profiles

Figure 2a shows the difference in summer NO_2 VCDs using the new daily profiles compared to the old v2.1C monthly profiles. Figure 4 shows the difference in v3.0A of the average total tropospheric NO_2 columns when using daily NO_2 profiles rather than monthly average profiles. Figure 4a is the summer (JJA) average, and shows a significant increase in VCDs along the eastern US, which is not present in the winter (DJF) average (Fig. 4b). The timing and location suggest that this difference is due to lightning, as the southeastern US especially has very active lightning (Laughner and Cohen, 2017; Travis et al., 2016; Hudman et al., 2007).

Ultimately, the fact that lightning is an intermittent but significant NO_x source in the upper troposphere (UT) is the cause of this difference. Figure 5a shows the statistical distribution of NO_2 in the UT for two regions in the US: the southeast, which has significant lightning activity, and the northwest, which has very little lightning. The distribution is highly skewed with a long tail in the southeastern US due to the lightning activity, but not in the northwestern US. Because of the nonlinear nature of the AMF calculation, this skewed distribution translates into different average VCD values.

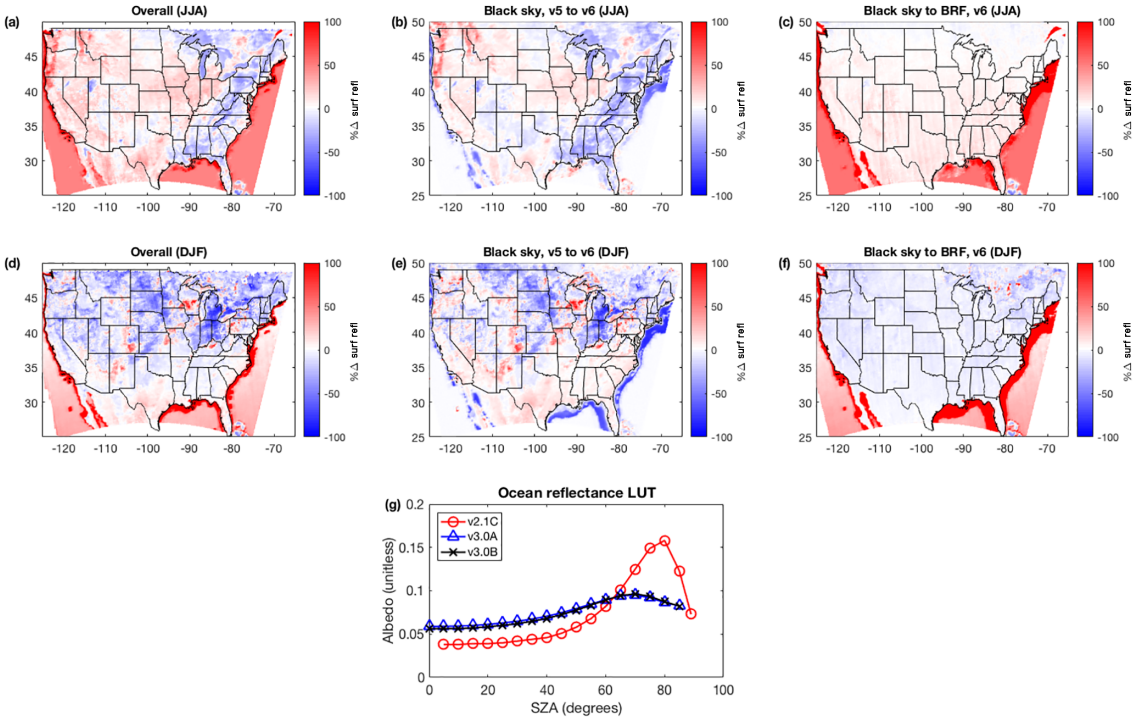

Figure 3. **(a, d)** Difference in surface reflectance between BEHR v2.1C (MODIS MCD43C3 black sky albedo, old ocean look-up table) and BEHR v3.0B (MODIS MCD43Dxx BRF, new look-up table). **(b, e)** Difference in surface reflectance between versions 5 and 6 of the MODIS black sky albedo (no change in ocean look-up table). **(c, f)** Difference in surface reflectance between the MODIS black sky and BRF product and the change in the ocean look-up table. **(a–c)** are for summer (JJA) and **(d–f)** are for winter (DJF). **(g)** The ocean albedo look-up table values for v2.1C, v3.0A, and v3.0B. (The change between v3.0A and v3.0B is discussed in Sect. 5.2.)

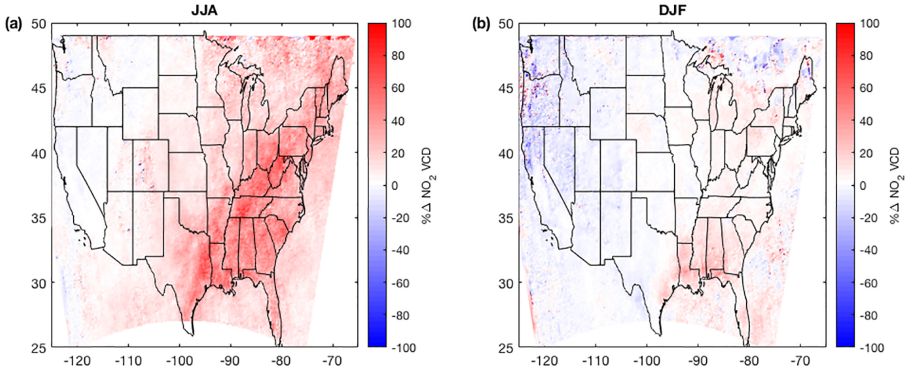

Figure 4. **(a, b)** Percent difference in v3.0A NO_2 VCDs using daily instead of monthly profiles averaged over **(a)** June–August and **(b)** January, February, and December 2012. Averages exclude pixels affected by the row anomaly and with cloud fraction > 0.2.

Figure 5, panels b and c, show average shape factors derived from monthly averaged and daily a priori profiles for the southeastern and northwestern US. A shape factor is a profile divided by its integral:

$$S(p) = \frac{g(p)}{\int_{p_{\text{surf}}}^{p_{\text{trop}}} g(p)\,\mathrm{d}p}. \tag{12}$$

A shape factor can be interpreted as the relative vertical distribution of NO_2. It appears implicitly in the AMF calculation (Eq. 2).

Here we see how the skewed UT NO_2 distribution affects the southeastern US AMFs through the shape factor. Figure 5b shows that the statistically skewed UT NO_2 distribution causes shape factors calculated from the monthly average a priori profiles in the southeastern US to have a larger fraction of the column NO_2 in the UT than that calculated

from the daily profiles. Through Eq. (2), this leads to systematically greater AMFs (and therefore smaller VCDs) in the southeast when using the monthly profiles if the scattering weights ($w(p)$ in Eq. 2) are greater in the UT than near the surface, which is usually the case. In contrast, Fig. 5c shows no difference in the monthly or daily shape factors for the northwestern US. For interested readers, a more mathematical argument is given in Sect. S2.

The implication is that, for regions with long-tailed statistical distributions of NO_2 concentrations, there will be systematic differences between a product using monthly average and daily a priori profiles. It is likely that the VCDs calculated using the daily a priori profiles are more accurate, because in theory daily a priori profiles should properly account for that long tail on days when it is relevant, whereas monthly profiles will average in the extreme values.

Finally we note that this difference between daily and monthly profiles may change in the future. Laughner et al. (2018e) found that the simulation providing the NO_2 profiles had too much lightning in the southeastern US. Correcting that may reduce the skewness of the UT NO_2 distribution. Work is underway to improve the representation of lightning for the southeastern US NO_2 profiles.

4.4 WRF-Chem temperature profiles

Simulated or recorded temperature profiles are necessary to correct for the temperature dependence of the NO_2 cross section (Sect. 2.1 of this paper, also Bucsela et al., 2013). BEHR v2.1C used temperature profiles provided to us by NASA at $5^\circ \times 2^\circ$ resolution (Bucsela et al., 2006). Recently, an error was identified in the temperature profile lookup used in BEHR v2.1C. Correcting this error changes the v2.1C VCDs by $-1.7\,\% \pm 3.8\,\%$ in the summer, and $-0.9\,\% \pm 11.2\,\%$ winter (Fig. S9). Therefore the impact was small in both seasons, but more variable in the winter.

BEHR v3.0A uses temperature profiles from WRF-Chem at 12 km resolution instead. The effect on total tropospheric VCDs is shown in Fig. 1d (monthly a priori profiles) and Fig. 2b (daily a priori profiles). It is small, $0.5\,\% \pm 0.4\,\%$ on average in summer using monthly average profiles. Using daily temperature profiles, the change is slightly more variable ($0.6\,\% \pm 0.5\,\%$). Therefore, high-resolution temperature profiles are significantly less important than NO_2 profiles, which is expected, as temperature should not vary as rapidly in space as NO_2.

4.5 Gridding method

BEHR v2.1C used a constant value method (CVM) gridding algorithm to oversample the native pixel data to a fixed $0.05^\circ \times 0.05^\circ$ grid. A constant value method assigns the VCD of a given pixel to any grid points within the pixel bounds; this works well when the grid resolution is significantly finer than the native pixel resolution. It was found that the existing algorithm was at times overly conservative, and did not assign values to grid cells near the border of two pixels.

BEHR v3.0A also uses a CVM gridding algorithm, however the implementation was changed. The new CVM algorithm is a slightly modified version of that provided by Kuhlmann et al. (2014), with a custom interface to allow communication between the Python code from https://github.com/gkuhl/omi (last access: 14 November 2018) and the BEHR Matlab code.

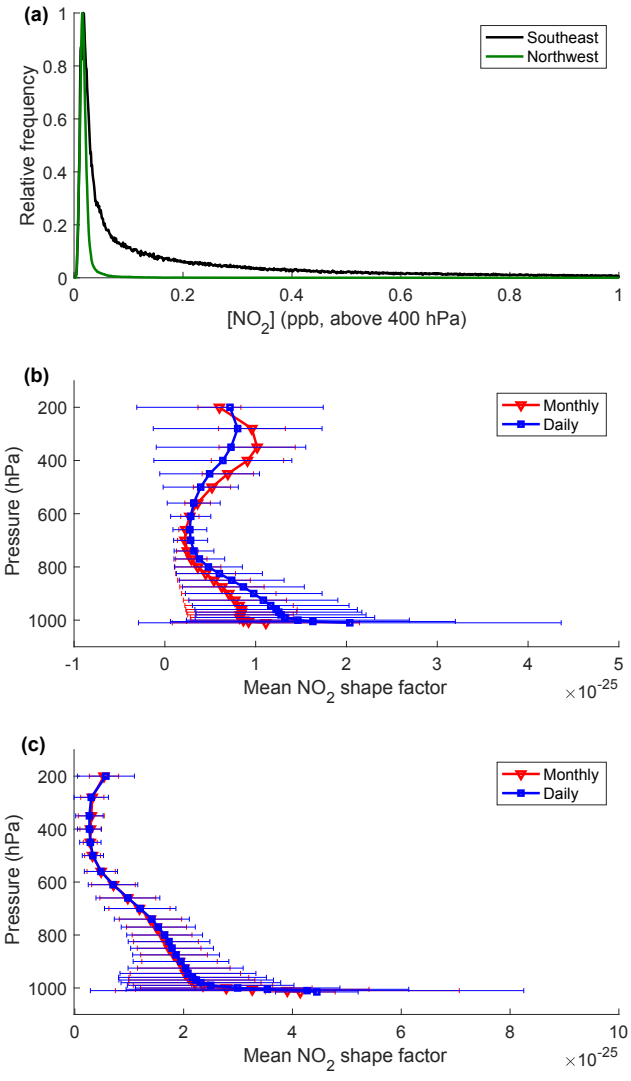

Figure 5. **(a)** Frequency distribution (normalized to maximum) of average NO_2 above 400 hPa in the a priori profiles for the southeastern and northwestern US, from June to August 2012. **(b, c)** Mean a priori NO_2 shape factors over the southeastern US **(b)** and northwestern US **(c)** for June–August 2012. Shape factors are defined as the NO_2 profile in a mixing ratio divided by its integral in molec. cm^{-2}. The error bars are $\pm 1\sigma$. The regions (southeastern and northwestern US) are shown in Fig. S4.

We also tested the parabolic spline method (PSM) of gridding described in Kuhlmann et al. (2014), with updates from Schütt (2017). The PSM attempts to recover maxima in NO_2 between adjacent pixels by fitting the NO_2 VCDs with 2-D splines and sampling the grid points along those splines. While this algorithm should be an ideal match with our retrieval (as our high-resolution profiles are able to better resolve urban–rural NO_2 gradients), two technical challenges persisted. First, non-physical oscillations in the NO_2 VCDs would appear, especially on the edge of the row anomaly. Second, in one test, the PSM algorithm resulted in much greater VCDs than the CVM algorithm over a large area. As this is not the expected behavior, v3.0A uses the new CVM method from Kuhlmann et al. (2014).

Figures 1e and 2c shows the percent change in the VCDs resulting from the change in gridding method for the subproducts using monthly and daily a priori profiles, respectively. The average effect is small and no spatial pattern is evident, as would be expected, although individual effects are quite variable (Table 3). The new CVM algorithm correctly assigns grid cells near the border of two pixels to one or the other. If two pixels overlap, an average of their values weighted by the inverse of their area (FoV75Area from the OMPIXCOR product) is assigned.

5 Changes in BEHR v3.0B

v3.0B implemented six main changes from v3.0A.

1. Retrievals using daily WRF-Chem profiles use the profile nearest in time to OMI overpass, rather than the last profile before the OMI overpass
2. Ocean surface reflectance calculated at 460 nm instead of 430 nm
3. Variable tropopause pressure (derived from WRF simulations) implemented in the AMF calculation
4. The method for calculating surface pressure from Zhou et al. (2009) was implemented
5. Clear and cloudy scattering weights are included separately in the native pixel files
6. The summary bits in the BEHRQualityFlags field were corrected.

Changes nos. 1–4 directly affect the retrieved VCDs. No. 5 is intended for advanced users who wish to implement custom profiles. No. 6 makes rejecting low-quality data easier for standard users.

5.1 Profile time effects

In v3.0A, when using daily profiles, the last set of profiles before the OMI overpass time was used. In v3.0B, this was changed to be the nearest profile in time. The overall average difference is near 0 (Fig. 2d, Tables 3 and 4), and the absolute magnitude of the average changes is $< 4 \times 10^{14}$ molec. cm^{-2}. As expected, a difference of 1 h in some of the selected profiles makes very little difference to the average retrieved column density.

5.2 Ocean surface reflectance LUT effects

Figures 1f and 2d show the changes to the NO_2 VCD (for the subproducts using monthly and daily a priori profiles, respectively) caused by the change to the wavelength of the ocean reflectance LUT and the selection of the closest profile in time. Figure 1f only shows the effect due to the ocean surface reflectance LUT, as the monthly a priori profiles are not affected by the change in how the closest daily profile in time is selected.

In v3.0A, the ocean surface reflectance was calculated at 430 nm as the approximate midpoint of the wavelength fitting window for an NO_2 retrieval (402–465 nm, Krotkov et al., 2017). In v3.0B, this was changed to be 460 nm, which is within the MODIS band used (459–479 nm). While both approaches have merit, we chose to move towards calculating the surface reflectance at similar wavelengths for consistency between the ocean and land data. The change in VCD retrieved over ocean is very small ($< 1\,\%$, Tables 3 and 4), as expected.

5.3 Implementation of variable tropopause height

BEHR v3.0B uses variable tropopause pressure derived from WRF simulations while in prior versions the tropopause pressure is set to be 200 hPa. Figures 1g and 2e reflect the effect of changes in tropopause pressure on NO_2 VCD. The changes in NO_2 are consistent with the variation in tropopause pressure. In summertime, the WRF-derived thermal tropopause pressure in lower latitudes ($< 45°$ N) is less than 200 hPa. This increases the contribution of the UT, where OMI is highly sensitive to NO_2, to the AMF, which in turn reduces the retrieved NO_2 VCDs. In higher latitudes ($> 45°$ N), the thermal tropopause pressure is greater than 200 hPa and leads to a slight increase in NO_2 VCD. The changes in average NO_2 VCD caused by changes in tropopause pressure are small, $-1.6\,\% \pm 5.3\,\%$ using monthly average profiles and $-1.1\,\% \pm 8.2\,\%$ using daily profiles. In wintertime, the WRF tropopause is below the previous 200 hPa value over most of the US and it causes a broad enhancement of NO_2 VCD in most US domain ($> 30°$ N) by approximately 2 % (Figs. S12, S15, Tables 3, 4). Evaluation of the tropopause pressure calculation is ongoing; the calculation of the tropopause pressure may be revised in future versions of BEHR.

5.4 Surface pressure calculation

Figures 1h and 2f show the impact of switching from a fixed scale height calculation to using the hypsometric equation to adjust WRF modeled surface pressure to the GLOBE terrain elevation. As expected, the changes are similar whether monthly or daily WRF output is used and are greatest over the Rocky and Appalachian mountains (up to a maximum of $\sim 10\,\%$). This is similar to the 5 % effect Zhou et al. (2009) found in the summer, indicating that the meteorological surface pressure correction in mountainous regions does impact the NO_2 columns even with a high-resolution terrain elevation database.

5.5 Publishing separate clear and cloudy scattering weights

Very advanced users may wish to recalculate custom AMFs using their own NO_2 profiles but with the scattering weights used in BEHR. To facilitate this, an array of scattering weights used in the BEHR AMF calculation is included in the published native pixel resolution files. In BEHR v3.0A and prior, these scattering weights were the cloud radiance fraction weighted average of the temperature-corrected clear and cloudy scattering weights:

$$w'(p) = (1 - f)w_{\text{clear}}(p)\alpha(p) + f\,w_{\text{cloudy}}(p)\alpha(p), \tag{13}$$

where $\alpha(p)$ is defined by Eq. (6) and $w_{\text{clear}}(p)$ and w_{cloudy} are set to 0 below the surface and cloud pressures, respectively.

Using these scattering weights along with the published a priori profiles, users could reproduce BEHR AMFs well, to within $0.5\,\% \pm 1.9\,\%$, using

$$A' = \frac{\int_{p_{\text{surf}}}^{p_{\text{trop}}} w'(p)g(p)\,\mathrm{d}p}{\int_{p_{\text{surf}}}^{p_{\text{trop}}} g(p)\,\mathrm{d}p}, \tag{14}$$

where $g(p)$ is the a priori profile also provided in the BEHR product. However, publishing the clear and cloudy weights separately increases the precision of reproduced AMFs by three orders of magnitude. Using these with the provided BEHR a priori profiles allows users to reproduce BEHR AMFs effectively exactly using Eq. (2) (Fig. S10). The primary purpose is to allow users to replace the BEHR NO_2 profiles with their own for a custom AMF calculation. In theory, this also permits advanced users to use different cloud fractions in their custom AMF calculations, but doing so would require careful attention to possible errors, as the scattering weights are tied to the cloud pressure used in BEHR.

5.6 BEHR quality flags

Starting with v3.0A, the BEHRQualityFlags field summarized key quality issues from both the NASA and BEHR processing steps. The first and second bits in these values are summary bits, so that users who want high-quality data can very easily identify such data. Due to a bug in v3.0A, these bits did not filter out all low-quality data. This has been rectified in v3.0B. See Sect. 7 for the proper use of these flags. These flags may be updated in the future if additional causes of low-quality NO_2 VCDs are identified. Users should be sure to check the changelog at http://behr.cchem.berkeley.edu/Portals/2/Changelog.txt (last access: 14 November 2018) for any changes to the flags. If the quality flags are updated, the BEHR version number will be incremented, either by a major version (e.g., v3.0B to v3.0C) or a minor revision (e.g., v3.0B to v3.0Brev1).

6 Overall difference

Overall, the two changes that had the largest impact on the retrieved VCDs were the new NASA slant column fitting and the new a priori NO_2 profiles ($-14\,\% \pm 14\,\%$ and $0.86\,\% \pm 20.14\,\%$, respectively, Table 3). Although the overall average effect of the new profiles is small, this is only because it causes both positive and negative changes to the VCDs. The large standard deviation reflects how different areas do have very significant changes. The effects of the a priori profiles were especially strong in the SE US where lightning has a strong influence on the profile shape in the summer (Fig. 6). Given the high sensitivity of NO_2 retrievals to upper tropospheric NO_2, this is not surprising. The omission of lightning NO_2 from the original BEHR product was a limitation of WRF-Chem at the time the product was created (Russell et al., 2012); lightning NO_x emission was not added to WRF-Chem until v3.5.0, released in April, 2013 (http://www2.mmm.ucar.edu/wrf/users/download/get_sources.html#WRF-Chem, last access: 14 November 2018). The change due to the SCD fitting resulted in a fairly uniform decrease in NO_2 VCDs across the domain.

The difference in the averages using daily (Fig. 6c, d) vs. monthly profiles (Fig. 6a, b) is variable. Laughner et al. (2016), did not see a significant difference in average VCDs using daily versus monthly a priori profiles. Those results were obtained using a model simulation without lightning. In regions without significant lightning, this is expected because averaging over time periods greater than a month eliminates the temporal variability captured by the daily profiles. However, when there is significant lightning, the skewed UT NO_2 distribution results in significant differences to the averages. The effect of the daily profiles is on the average strongest in the SE US, as discussed in Sect. 4.3.2, and is still an overall decrease compared to the v2.1C profiles, due to the inclusion of lightning and the reduction in surface emissions.

It should be noted that the difference between retrievals with daily and monthly profiles will be greater in years other than 2012, since the daily profiles incorporate year-specific emissions, while monthly profiles always assume 2012 anthropogenic emissions.

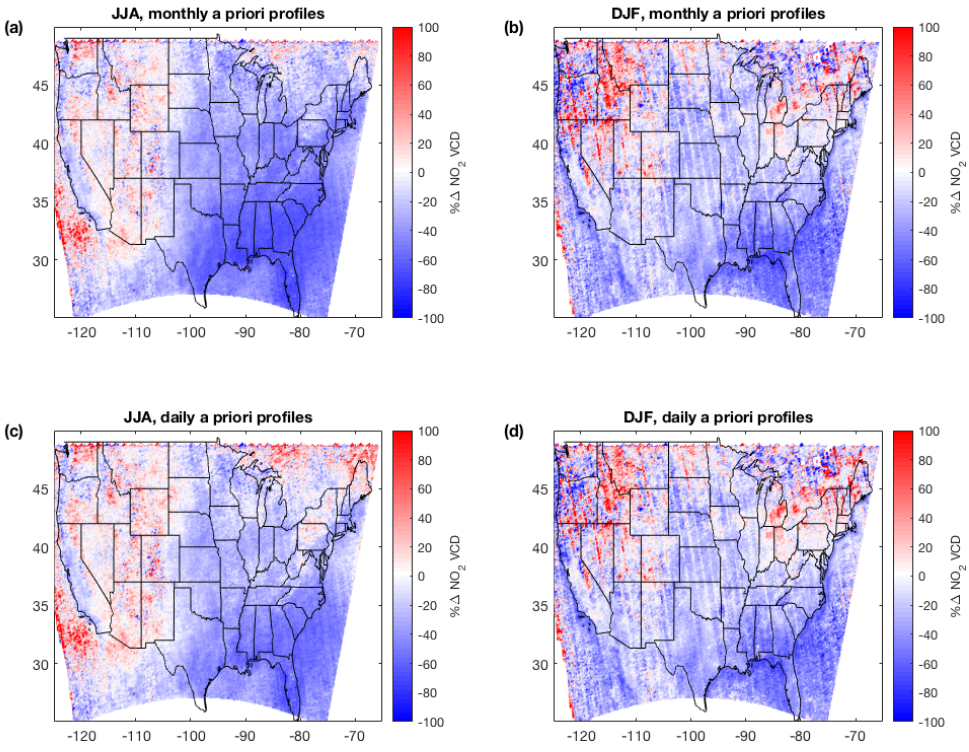

Figure 6. Overall average differences in total tropospheric NO_2 VCDs between v2.1C and v3.0B for June–August **(a, c)** and January, February, December **(b, d)** of 2012. **(a, b)** using monthly NO_2 profiles in v3.0B, **(c, d)** using daily profiles in v3.0B.

7 Recommendations for use

In our experience, the most common use of the BEHR data falls into three categories:

1. Direct use of the NO_2 VCDs for various purposes, including calculation of NO_2 trends, direct inference of lightning or other emissions, etc.
2. Inverting the VCDs to obtain surface NO_2 concentrations
3. Comparing the BEHR VCDs to modeled VCDs to evaluate the model, infer emissions by constraining the model, etc.

Here we will give a brief summary of recommendations to use BEHR for each of these applications, as well as general recommendations that apply to all uses of the data.

7.1 General recommendations

7.1.1 Quality filtering

It is vital in any use of BEHR data to filter out low-quality data. The BEHR algorithm attempts to calculate an NO_2 VCD for as many pixels as possible, even if some of those pixels are known to be of poor quality. The philosophy is that it is better to have data for a pixel if at all possible and to remove it only if the quality is too low for a particular application. Some causes of low quality (e.g., the row anomaly, https://projects.knmi.nl/omi/research/product/rowanomaly-background.php, last access: 14 November 2018) make the NO_2 column unusable in any case, while others (e.g., high cloud fraction, low-quality surface reflectance) only affect certain uses.

The quality of the pixel is summarized in the first two (least-significant) bits of the BEHRQualityFlags field. The second bit is a critical error bit, if set (i.e., if a bitwise AND of BEHRQualityFlags with 2 is > 0) then the NO_2 columns for that pixel should not be used under any conditions. The first bit is a quality flag bit; if it is set (if a bitwise AND of BEHRQualityFlags with 1 is > 0) then the use of the column for typical applications wanting information down to the surface is not recommended; however, other applications may still find use for this pixel. For example, the first bit is set if the OMI geometric cloud fraction is > 0.2, since the uncertainty of the total tropospheric column increases greatly as more NO_2 is obscured by clouds, but cloud slicing ap-

proaches (e.g., Choi et al., 2014; Marais et al., 2018) will actually prefer large cloud fractions, and so will need to do their own cloud filtering. For most applications however, it is recommended to ignore pixels that have the first (i.e., quality summary) bit set to 1.

Users must also be sure to remove fill values. The fill value for each field is defined in the "fillvalue" attribute. Generally, checking whether a value is exactly equal to a fill value is not recommended unless the value is an integer type, as floating point error on some systems may cause fill values to be missed. It is better practice to check for values within some relative tolerance of the fill value:

$$|x - f| < |f| \cdot t, \tag{15}$$

where x is the data, f the fill value, and t the tolerance. $t = 10^{-4}$ works in our experience.

7.1.2 Choice of daily or monthly profile subproduct

Users will also need to choose whether to use the subproduct with daily profiles. Use of the subproduct with daily profiles is strongly encouraged if possible, for two reasons. First, the daily profiles also use year-specific emissions (Sect. 2.6.1), and so will better capture trends in VCDs as the surface contribution to the a priori profiles is reduced. Second, Laughner et al. (2016) showed that using daily profiles significantly changes day-to-day VCDs, and that some applications of satellite data can be biased when monthly profiles are used. Applications similar to those studied in Laughner et al. (2016), where upwind or downwind columns are systematically averaged together, are particularly vulnerable to bias when monthly average profiles are used.

Caution is advised if comparing 2005 or 2006 data using daily profiles to other years; the different WRF-Chem boundary conditions (Sect. 2.6.1) may also bias observed trends. This effect is likely small, as in a test of 1 week of data using two sets of profiles, one using GEOS-Chem boundary conditions and one using MOZART boundary conditions, the mean change was $< 10^{14}$ molec. cm^{-2}, and only 0.7 % of pixels with any cloud fraction had a change exceeding 1×10^{15} molec. cm^{-2} (0.05 % of pixels with cloud fraction < 0.2).

Mixing daily and monthly profile subproducts is *strongly* discouraged, as systematic differences between them (i.e., Sect. 4.3.2 of this paper; Laughner et al., 2016) will bias any trends observed.

7.2 Application no. 1: direct observation of VCDs

Direct observation of VCDs has a number of applications, including elucidating trends in NO_2 burdens (e.g., Russell et al., 2012; Jiang et al., 2018) or inferring lightning emissions (e.g., Pickering et al., 2016). Users wanting to average BEHR data over a given time period, e.g., to compare summer average NO_2 columns for different years, will find this easiest using the gridded data, as this places the NO_2 columns on a consistent equirectangular latitude–longitude grid (i.e., the data in grid cell (1,1) will be at the same lat–lon in each orbit, whereas in the native data, pixel (1,1) will not), so it is easy to average across different days. When averaging, each grid cell should be weighted by the area weight value given in the gridded product; this is the inverse of the pixel area, so weighting by this inherently gives more weight to smaller, more representative pixels.

Users interested in VCDs from individual days (e.g., to find NO_2 downwind of an episodic event such as lightning) can use either the native pixel or gridded products, whichever is easier. In this case, it is important to keep in mind that pixel sizes vary from day to day. Therefore, if the source signal of interest is smaller than a single pixel, it will be more diluted if it falls in a larger pixel on the edge of the OMI swath than a small one near the center.

7.3 Application no. 2: inferring surface NO_2 concentration

Since a VCD is a measurement integrated over the troposphere, it does not directly provide information about the surface concentration of NO_2. The simplest approach to infer ground-level NO_2 concentrations from VCDs is to multiply the BEHR VCD by the ratio of surface concentration to VCD obtained from a modeled NO_2 profile (Lamsal et al., 2008):

$$[NO_2]_{surf} = \frac{g\,(p_{surf})}{\int_{p_{surf}}^{p_{trop}} g(p)\,\mathrm{d}p} V_{BEHR}, \tag{16}$$

where $g(p)$ is the modeled profile, p_{surf} the surface press, p_{trop} the tropopause pressure, and V_{BEHR} the BEHR VCD. $g(p)$ may be obtained in many ways; for users without model output or measurements of NO_2 profiles, the a priori profiles used in BEHR are included in the native pixel subproduct and may be used for this purpose. In this case, using the subproduct with daily profiles is highly recommended so that the profiles respond to changes in meteorology day to day, especially wind fields.

7.4 Application no. 3: comparing to models

Users wishing to compare BEHR VCDs to model output should follow the suggestions in Boersma et al. (2016). This requires calculating the overlap between the BEHR pixels and the user's model grid cells and applying the BEHR averaging kernel to the user's model profile before calculating the model VCD, so the native pixel product must be used, since it contains the averaging kernels and the pixel corners.

The averaging kernels would be applied to the model profile as

$$V_{model} = \sum_k c_k a_k, \tag{17}$$

where V_{model} is the modeled VCD after applying the averaging kernels, k is the level index, c_k is the model profile converted to a partial column for level k, and a_k is the averaging kernel for level k.

There are three important considerations in this application. First, since BEHR provides only a tropospheric VCD, it must be compared against a modeled tropospheric column, no stratospheric component may be included.

Second, the model NO_2 profile should be interpolated to the pressure levels on which the averaging kernels are defined (given in the BEHR files as BEHRPressureLevels) rather than the other way around. This is because the averaging kernels may have sharp changes between levels (usually at the cloud pressure, since OMI's sensitivity increases dramatically over a bright cloud), so interpolating the averaging kernels to the model pressures is more likely to introduce errors.

Third, the model profile is best converted to partial columns before applying the averaging kernels. This may be done in several ways, such as the following.

- Interpolate the profile to the averaging kernels' pressure levels, then multiply the profile concentration as number density by the layer height.
- Interpolate the profile to the *edges* of the averaging kernels' levels, then integrate over each layer to obtain the partial column.

Both methods need the edge of the pressure levels, either to calculate the box height or to define the limits of the integration. Since the pressures given for the averaging kernels are the level centers, the edges are most easily defined as the midpoints between those layers; with the surface pressure serving as the lower limit of the bottom layer and the tropopause pressure serving as the upper limit of the top layer.

Converting from pressure to altitude for either method can either be done using a scale height relation (e.g., Eq. 10), though this will likely introduce some error as we saw in Sect. 5.4 that the meteorological correction can be significant. A better option, if the user's model output includes altitude and pressure vectors, is to interpolate the altitude from the model to the averaging kernels' pressure levels alongside the NO_2. Alternatively, in the second method, NO_2 profiles in mixing ratio can be directly integrated over pressure (Ziemke et al., 2001, Appendix B). This is done internally in BEHR using the integPr2 code at https://github.com/CohenBerkeleyLab/BEHR-core-utils/blob/develop/AMF_tools/integPr2.m (last access: 14 November 2018).

8 Code and data availability

BEHR data are stored in monthly compressed files as four subproducts on the University of California DASH archive (Laughner et al., 2018a, b, c, d). All BEHR data are also available for download at http://behr.cchem.berkeley.edu (last access: 14 November 2018). The BEHR code is hosted on GitHub at https://github.com/CohenBerkeleyLab/BEHR-core/tree/master (last access: 14 November 2018) (Laughner and Zhu, 2018b). WRF-Chem simulations for 2005–10, and 2012–2014 are available at the time of writing. Full model output is available for 2005, 2007–2009, and 2012–2014; a reduced set of variables is stored for 2006 and 2010 to save space. Due to the large file size, access currently must be arranged by contacting the corresponding author; work is underway to make it available through http://behr.cchem.berkeley.edu/. The analysis code for this paper (and its dependencies) along with the incremental averages are available at https://doi.org/10.5281/zenodo.1247564 (Laughner and Zhu, 2018a).

The v3.0 NASA Aura OMI NO_2 standard product (Krotkov and Veefkind, 2016) and OMI/Aura Ground Pixel Corners product (Kurosu and Celarier, 2010) was obtained from the Goddard Earth Science Data and Information Services Center (GES DISC) in Greenbelt, MD, USA. The MODIS Aqua Clouds 5-Min L2 Swath 1 and 5 km (MYD06_L2 Platnick et al., 2015) and MODIS Terra+Aqua BRDF/Albedo Parameters 1–3 Band3 and QA BRDF Quality Daily L3 Global 30ArcSec CMG V006 (Schaaf, 2015a, b, c, d, MCD43D07, MCD43D08, MCD43D09, MCD43D31) were acquired from the Level-1 and Atmospheric Archive and Distribution System (LAADS) Distributed Active Archive Center (DAAC) located in the Goddard Space Flight Center in Greenbelt, MD (https://ladsweb.nascom.nasa.gov/, last access: 14 November 2018).

9 Conclusions

Here we present v3.0 of the Berkeley High Resolution OMI NO_2 product (BEHR NO_2). This version incorporates a number of changes, including updated a priori NO_2 profiles with lightning NO_x emissions, daily NO_2 profiles for select years, a directional surface reflectance product, variable tropopause height, a new gridding algorithm, and improved surface pressure calculation, in addition to using the current NASA OMI NO_2 Standard Product. The new a priori profiles and the upgrade to the new NASA product had the largest effect on the retrieved total tropospheric VCDs. Retrieved visible-only tropospheric VCDs were most strongly affected by the new visible-only AMF formulation, but otherwise were similarly affected by each change.

Appendix A: Published format

A1 File structure

BEHR data are published as HDF version 5 files. Each file contains a single, top-level group "Data", which in turn contains each orbit as a child group named "SwathX" where X is the orbit number. The datasets for each orbit are contained in the "SwathX" groups.

Separate HDF files contain data at the native OMI pixel resolution and regridded to $0.05° \times 0.05°$ resolution. The regridded files only contain a subset of the variables stored in the native pixel files. The regridded files contain each orbit gridded separately; each orbit's grid covers the entire domain retrieved. Grid cells outside each orbit's observed swath contain fill values. Users can identify whether a file contains gridded information by the dataset level attribute "gridding_method", if present, the file is a gridded file; if absent, the file is a native pixel file. Additionally, the "Description" attribute contained in each swath indicates whether the data are at native or regridded resolution.

Retrievals using daily vs. monthly NO_2 a priori profiles are available separately. Retrievals using monthly profiles will be updated as new OMI and MODIS data becomes available. Retrievals using daily profiles are limited by the need to model said profiles; these will become available as modeled NO_2 profiles are simulated.

BEHR files are named with the format "OMI_BEHR-*profile_region_version_yyyymmdd*.hdf", where:

- *profile* will be DAILY or MONTHLY, indicating whether daily or monthly NO_2 a priori profiles were used
- *region* region retrieved, currently, US = continental United States.
- *version* is the version string (Sect. A4).
- *yyyymmdd* is the date of the observation

This information is also contained as swath level attributes "BEHRProfileMode", "BEHRRegion", "Version", and "Date", respectively.

A2 Key variables

The BEHR files contain a large number of variables, including a large amount of ancillary data used in the algorithm. All variables in the HDF files have a "description" attribute that provides some information about what they are. They also have a "product" attribute that indicates whether they are taken verbatim from the NASA Standard Product (product = "SP") or added by BEHR (product = "BEHR"). The primary variables that most users should focus on are:

- *BEHRColumnAmountNO2Trop*: this is the tropospheric VCD calculated using Eqs. (1) and (2). It is the concentration of NO_2 integrated from the surface to the tropopause, including NO_2 below clouds. This is the NO_2 value that most users should use. *Historical note:* the BEHR v2.1A documentation indicated that this was a visible-only VCD; that was incorrect. This value has been the total tropospheric column in all BEHR versions.
- *BEHRColumnAmountNO2TropVisOnly*: this is the visible-only tropospheric VCD calculated with Eqs. (1) and (3). It excludes below-cloud NO_2. Generally the use for this quantity is more specialized; most users should use the previous value.
- *BEHRQualityFlags*: a 32-bit unsigned integer value where each bit represents a boolean flag indicating the presence of a specific error or warning for that pixel. See Sect. A3 for details.
- *Areaweight* (*gridded products only*): a weight calculated of the inverse of the area of the pixel that each grid cell falls within. This should be used to weight the gridded data during temporal averaging (see Sect. 7).
- *Longitude*, *Latitude*: the coordinates of the pixel or grid cell center.
- *CloudFraction*: this is a geometric cloud fraction from the OMI O_2–O_2 cloud product (Acarreta et al., 2004). It is the default used to filter for cloudy pixels, and is the same as the corresponding variable in the NASA Standard Product.
- *CloudRadianceFraction*: this is a radiance cloud fraction (i.e., one weighted by the amount of light coming from the cloud vs. the ground). It is the same as the corresponding field in the NASA Standard Product.
- *MODISCloud*: this is a geometric cloud fraction from the Aqua MODIS instrument (Platnick et al., 2015) averaged to the OMI pixels. It is an alternate way of filtering for cloudy pixels that may be less susceptible to false positives from highly reflective ground (Russell et al., 2011). Some pixels near the edge of the swath may be missing this data since the MODIS swath width is slightly smaller than OMI's.

More advanced users may find the 3-D variables included in the native pixel subproducts useful. These variables give a unique vector of values for each pixel. In Matlab, the vector for each pixel runs along the first dimension, so if the NO_2 VCDs are the 2-D array `V` and one of the 3-D arrays is `A`, then the vector corresponding to `V(i,j)` would be `A(:,i,j)`. However, some languages reverse the order of the dimensions. In BEHR v3.0B, the vector dimension can be identified as the one with a length of 33.

In BEHR, these 3-D variables are defined on a vertical grid of 30 standard pressure levels (ranging from 1020 to 60 hPa)

with values interpolated to the surface pressure, cloud pressure, and tropopause pressure included, bringing the total length of the vertical dimension to 33. If one of the interpolated pressure levels is the same as a standard pressure level, the value is not duplicated, and the vector of values will be padded with fill values at the end.

- *BEHRPressureLevels*: this dataset defines the pressure levels that the other 3-D variables are defined on.
- *BEHRNO2apriori*: this dataset gives the NO_2 a priori profiles used in the BEHR retrieval in mixing ratio.
- *BEHRAvgKernels*: these are the averaging kernels referenced in Sect. 7.4. They are defined as

$$a(p) = \frac{(1-f)w_{\text{clear}}(p)\alpha(p) + f\,w_{\text{cloudy}}(p)\alpha(p)}{A}, \quad \text{(A1)}$$

  where $a(p)$ is the averaging kernel, f the cloud radiance fraction, $\alpha(p)$ the temperature correction (Eq. 6) A the BEHR AMF, and $w_{\text{clear}}(p)$ and $w_{\text{cloudy}}(p)$ the clear and cloudy scattering weights, which are set to 0 below the surface and cloud pressure, respectively.
- *BEHRScatteringWeightsClear*, *BEHRScatteringWeightsCloudy*: the temperature corrected clear and cloudy scattering weights, set to 0 below the surface and cloud pressure, respectively, i.e.,

$$w'_{\text{clear}}(p) = w_{\text{clear}}(p)\alpha(p), \quad \text{(A2)}$$
$$w'_{\text{cloudy}}(p) = w_{\text{cloudy}}(p)\alpha(p). \quad \text{(A3)}$$

A3 Quality flagging

BEHR data contains a 32-bit unsigned integer quality flag field that summarizes quality errors and warnings from both the NASA processing and BEHR processing. Each bit in the integer value represents a specific error or warning flagged during processing. The bits are divided into three categories; the bit number is the position of the bit (1-based) starting from the least significant bit.

- *Bits 1 and 2: summary bits.* These summarize the other 30 bits. Users interested in simple filtering can focus only on these.
- *Bits 3–16: error bits.* These are set to 1 for significant errors in the retrieval that preclude the use of the corresponding NO_2 data in any capacity.
- *Bits 17–32: warning bits.* These are set to 1 as nonfatal warnings about the processing of the corresponding data. These do not automatically preclude the use of the corresponding data, but rather provide warnings of potentially lower-quality data or information about decisions made during the retrieval. The flags for low-quality BRF data (Sect. 2.2) fall into this category.

The meaning of each used bit is given in the "FlagMeanings" attribute of the BEHRQualityFlags dataset; here, we will only discuss the two summary bits.

Bit 2 is the error summary bit; it is set to 1 if any error bit is set. Therefore, NO_2 columns from any pixel with this bit set should not be used. In v3.0B, this is set if the NASA VcdQualityFlags or XTrackQualityFlags fields indicate the pixel should not be used, or if the BEHR AMF is invalid (usually because a WRF profile is not available for that pixel).

Bit 1 is the quality summary bit; in v3.0B, it is set to 1 if bit 2 is set, the MODIS BRF coefficients are of low quality, or the OMI geometric cloud fraction exceeds 20 %. Therefore, the NO_2 data can be restricted to high-quality, total tropospheric column data by using only pixels where this bit is not set.

As an example, if a pixel is in the row anomaly, then the 5th bit will be set, which also requires bits 1 and 2 to be set. The (little-endian) binary representation for this pixel would be 11001 (followed by 0s), so the value stored would be $2^0 + 2^1 + 2^4 = 19$. The easiest way to figure out if the nth bit is set is to do a bitwise AND operation between the quality flag value and 2^{n-1}, for $n \in [1, 32]$.

These quality flags focus on the quality of the NO_2 retrieval; therefore ancillary data (such as the MODIS surface reflectance or MODIS clouds) is not necessarily unusable for pixels flagged with a retrieval error.

In the gridded product, the quality flags field is a bitwise OR of all contributing pixels' quality flags. Therefore, any error or warning in a pixel that contributes to a grid cell is propagated to the grid cell.

A4 Versioning

BEHR versions follow the format "vX-XYrevZ", e.g., v3-0Arev0. The "X-X" indicates the version of the NASA Standard Product that was ingested as the basis for that BEHR retrieval. "Y" is a sequential letter (A, B, C, etc.) indicating the major version of BEHR produced from the same NASA SP base; i.e., v3-0A indicates the first major BEHR version based on the NASA SPv3. "revZ" (short for "revision") indicates a small update to the BEHR product. Revisions are reserved for small changes that are not expected to significantly affect scientific results obtained from the data, e.g., updates to file format or attributes, or very uncommon error corrections. A revision of 0 may be omitted from the version string; i.e., "v3-0A" and "v3-0Arev0" are the same version.

A5 Traceability

To ensure traceability, files ingested during processing from other satellite products or models are recorded in the swath level attributes "OMNO2File" (NASA NO_2 SP data), "OMPIXCORFile" (pixel corner data), "MODISCloudFiles" (MYD06 files that MODIS cloud data are taken from), "MODISAlbedoFile" (MCD43Dxx files that BRF parame-

ters are taken from), and "BEHRWRFFile" (WRF-Chem output files the NO_2 profiles are taken from are post-processed for monthly average profiles).

The BEHR code is available on GitHub at https://github.com/CohenBerkeleyLab/BEHR-core (Laughner and Zhu, 2018b). Each release will be tagged with the same version string as the data. Additionally, 11 swath level attributes contain the Git SHA-1 hash of the most recent commit of the core BEHR code and additional dependencies at the time each of the three major steps in processing BEHR data is executed. These attribute names have the form "GitHead_*repo_step*", where *repo* will be one of

- *Core*: the core BEHR repository (https://github.com/CohenBerkeleyLab/BEHR-core, last access: 14 November 2018),
- *BEHRUtils*: the repository of BEHR satellite utility functions (https://github.com/CohenBerkeleyLab/BEHR-core-utils, last access: 14 November 2018),
- *GenUtils*: the repository of general Matlab utilities (https://github.com/CohenBerkeleyLab/Matlab-Gen-Utils, last access: 14 November 2018),
- *PSM*: the repository containing the modified "omi" Python package used for gridding (https://github.com/CohenBerkeleyLab/BEHR-PSM-Gridding, last access: 14 November 2018),
- *MatPyInt*: the Matlab–Python type conversion interface (https://github.com/CohenBerkeleyLab/MatlabPythonInterface, last access: 14 November 2018), and
- *WRFUtils*: the repository containing Matlab utilities for working with WRF data (https://github.com/CohenBerkeleyLab/WRF_Utils, last access: 14 November 2018),

and *step* will be one of

- *Read*: step in which OMI, MODIS, and GLOBE data are ingested into Matlab and (where necessary) averaged to OMI pixels,
- *Main*: step in which scattering weights and NO_2 profiles are matched to OMI pixels, the BEHR AMFs and VCDs are calculated, and the data are gridded, and
- *Pub*: step in which the BEHR Matlab files are converted to HDF files.

Supplement. The supplement related to this article is available online at: https://doi.org/10.5194/essd-10-2069-2018-supplement.

Author contributions. JLL, QZ and RCC articulated a vision for a new BEHR algorithm. JLL and QZ converted those ideas to the code of the BEHR algorithm; JLL led the writing of the manuscript with input from QZ and RCC. RCC provided guidance and mentoring throughout the project and secured funding. All the authors reviewed the manuscript.

Competing interests. The authors declare that they have no conflict of interest.

Acknowledgements. The authors gratefully acknowledge support from NASA ESS Fellowship NNX14AK89H, NASA grant NNX15AE37G, and TEMPO project grant SV3-83019.

We would like to acknowledge high-performance computing support from Cheyenne (https://doi.org/10.5065/D6RX99HX) provided by NCAR's Computational and Information Systems Laboratory, sponsored by the National Science Foundation. This research also used the Savio computational cluster resource provided by the Berkeley Research Computing program at the University of California, Berkeley (supported by the UC Berkeley Chancellor, Vice Chancellor for Research, and Chief Information Officer).

We acknowledge use of WRF-Chem preprocessor tools MOZBC, fire_emiss, etc., provided by the Atmospheric Chemistry Observations and Modeling (ACOM) laboratory of NCAR. We also thank Eric Bucsela and Jim Gleason for very helpful discussions about the new formulation of the visible-only AMF.

Edited by: David Carlson
Reviewed by: two anonymous referees

References

Acarreta, J. R., De Haan, J. F., and Stammes, P.: Cloud pressure retrieval using the O_2-O_2 absorption band at 477 nm, J. Geophys. Res., 109, D05204, https://doi.org/10.1029/2003JD003915, 2004.

Anderson, D. C., Loughner, C. P., Diskin, G., Weinheimer, A., Canty, T. P., Salawitch, R. J., Worden, H. M., Fried, A., Mikoviny, T., Wisthaler, A., and Dickerson, R. R.: Measured and modeled CO and NO_y in DISCOVER-AQ: An evaluation of emissions and chemistry over the eastern US, Atmos. Environ., 96, 78–87, https://doi.org/https://doi.org/10.1016/j.atmosenv.2014.07.004, 2014.

Bechle, M. J., Millet, D. B., and Marshall, J. D.: National Spatiotemporal Exposure Surface for NO_2: Monthly Scaling of a Satellite-Derived Land-Use Regression, 2000–2010, Environ. Sci. Technol., 49, 12297–12305, https://doi.org/10.1021/acs.est.5b02882, 2015.

Beirle, S., Platt, U., Wenig, M., and Wagner, T.: NO_x production by lightning estimated with GOME, Adv. Space Res., 34, 793–797, https://doi.org/10.1016/j.asr.2003.07.069, 2004.

Beirle, S., Huntrieser, H., and Wagner, T.: Direct satellite observation of lightning-produced NO_x, Atmos. Chem. Phys., 10, 10965–10986, https://doi.org/10.5194/acp-10-10965-2010, 2010.

Beirle, S., Boersma, K., Platt, U., Lawrence, M., and Wagner, T.: Megacity Emissions and Lifetimes of Nitrogen Oxides Probed from Space, Science, 333, 1737–1739, 2011.

Belmonte Rivas, M., Veefkind, P., Boersma, F., Levelt, P., Eskes, H., and Gille, J.: Intercomparison of daytime stratospheric NO_2 satellite retrievals and model simulations, Atmos. Meas. Tech., 7, 2203–2225, https://doi.org/10.5194/amt-7-2203-2014, 2014.

Boersma, F., Bucsela, E., Brinksma, E., and Gleason, J. F.: NO_2, in: OMI Algorithm Theoretical Basis Document, edited by: Chance, K., Smithsonian Astrophysical Observatory, vol. IV: OMI Trace Gas Algorithms, Report #: ATBD-OMI-02 Version 2.0, 13–36, available at: https://ozoneaq.gsfc.nasa.gov/media/docs/ATBD-OMI-04.pdf (last access: 14 November 2018), 2001.

Boersma, K. F., Eskes, H. J., Dirksen, R. J., van der A, R. J., Veefkind, J. P., Stammes, P., Huijnen, V., Kleipool, Q. L., Sneep, M., Claas, J., Leitão, J., Richter, A., Zhou, Y., and Brunner, D.: An improved tropospheric NO_2 column retrieval algorithm for the Ozone Monitoring Instrument, Atmos. Meas. Tech., 4, 1905–1928, https://doi.org/10.5194/amt-4-1905-2011, 2011.

Boersma, K. F., Vinken, G. C. M., and Eskes, H. J.: Representativeness errors in comparing chemistry transport and chemistry climate models with satellite UV-Vis tropospheric column retrievals, Geosci. Model Dev., 9, 875–898, https://doi.org/10.5194/gmd-9-875-2016, 2016.

Boucher, O., Randall, D., Artaxo, P., Bretherton, C., Feingold, G., Forster, P., Kerminen, V.-M., Kondo, Y., Liao, H., Lohmann, U., Rasch, P., Satheesh, S., Sherwood, S., Stevens, B., and Zhang, X.: Climate Change 2013: The Physical Science Basis. Contribution of Working Group I to the Fifth Assessment Report of the Intergovernmental Panel on Climate Change, edited by: Stocker, T. F., Qin, D., Plattner, G.-K., Tignor, M., Allen, S. K., Boschung, J., Nauels, A., Xia, Y., Bex, V., and Midgley, P. M., Cambridge University Press, Cambridge, United Kingdom and New York, NY, USA, chap.: Clouds and Aerosols, 571–657, 2013.

Bousserez, N.: Space-based retrieval of NO_2 over biomass burning regions: quantifying and reducing uncertainties, Atmos. Meas. Tech., 7, 3431–3444, https://doi.org/10.5194/amt-7-3431-2014, 2014.

Browne, E. C., Perring, A. E., Wooldridge, P. J., Apel, E., Hall, S. R., Huey, L. G., Mao, J., Spencer, K. M., Clair, J. M. St., Weinheimer, A. J., Wisthaler, A., and Cohen, R. C.: Global and regional effects of the photochemistry of $CH_3O_2NO_2$: evidence from ARCTAS, Atmos. Chem. Phys., 11, 4209–4219, https://doi.org/10.5194/acp-11-4209-2011, 2011.

Browne, E. C., Wooldridge, P. J., Min, K.-E., and Cohen, R. C.: On the role of monoterpene chemistry in the remote continental boundary layer, Atmos. Chem. Phys., 14, 1225–1238, https://doi.org/10.5194/acp-14-1225-2014, 2014.

Bucsela, E., Celarier, E., Wenig, M., Gleason, J., Veefkind, J., Boersma, K., and Brinksma, E.: Algorithm for NO_2 vertical column retrieval from the ozone monitoring instrument, IEEE T. Geosci. Remote, 44, 1245–1258, https://doi.org/10.1109/tgrs.2005.863715, 2006.

Bucsela, E. J., Krotkov, N. A., Celarier, E. A., Lamsal, L. N., Swartz, W. H., Bhartia, P. K., Boersma, K. F., Veefkind, J. P.,

Gleason, J. F., and Pickering, K. E.: A new stratospheric and tropospheric NO_2 retrieval algorithm for nadir-viewing satellite instruments: applications to OMI, Atmos. Meas. Tech., 6, 2607–2626, https://doi.org/10.5194/amt-6-2607-2013, 2013.

Bucsela, E. J., Perring, A. E., Cohen, R. C., Boersma, K. F., Celarier, E. A., Gleason, J. F., Wenig, M. O., Bertram, T. H., Wooldridge, P. J., Dirksen, R., and Veefkind, J. P.: Comparison of tropospheric NO_2 from in situ aircraft measurements with near-real-time and standard product data from OMI, J. Geophys. Res., 113, D16S31, https://doi.org/10.1029/2007JD008838, 2008.

Bucsela, E. J., Pickering, K. E., Huntemann, T. L., Cohen, R. C., Perring, A., Gleason, J. F., Blakeslee, R. J., Albrecht, R. I., Holzworth, R., Cipriani, J. P., Vargas-Navarro, D., Mora-Segura, I., Pacheco-Hernández, A., and Laporte-Molina, S.: Lightning-generated NOx seen by the Ozone Monitoring Instrument during NASA's Tropical Composition, Cloud and Climate Coupling Experiment (TC^4), J. Geophys. Res., 115, D00J10, https://doi.org/10.1029/2009JD013118, 2010.

Burnett, R., Chen, H., Szyszkowicz, M., Fann, N., Hubbell, B., Pope, C. A., Apte, J. S., Brauer, M., Cohen, A., Weichenthal, S., Coggins, J., Di, Q., Brunekreef, B., Frostad, J., Lim, S. S., Kan, H., Walker, K. D., Thurston, G. D., Hayes, R. B., Lim, C. C., Turner, M. C., Jerrett, M., Krewski, D., Gapstur, S. M., Diver, W. R., Ostro, B., Goldberg, D., Crouse, D. L., Martin, R. V., Peters, P., Pinault, L., Tjepkema, M., van Donkelaar, A., Villeneuve, P. J., Miller, A. B., Yin, P., Zhou, M., Wang, L., Janssen, N. A. H., Marra, M., Atkinson, R. W., Tsang, H., Quoc Thach, T., Cannon, J. B., Allen, R. T., Hart, J. E., Laden, F., Cesaroni, G., Forastiere, F., Weinmayr, G., Jaensch, A., Nagel, G., Concin, H., and Spadaro, J. V.: Global estimates of mortality associated with long-term exposure to outdoor fine particulate matter, P. Natl. Acad. Sci. USA, 115, 9592–9597, https://doi.org/10.1073/pnas.1803222115, 2018.

Burrows, J. P., Weber, M., Buchwitz, M., Rozanov, V., Ladstätter-Weißenmayer, A., Richter, A., DeBeek, R., Hoogen, R., Bramstedt, K., Eichmann, K.-U., and Eisinger, M.: The Global Ozone Monitoring Experiment (GOME): Mission Concept and First Scientific Results, J. Atmos. Sci., 56, 151–175, https://doi.org/10.1175/1520-0469(1999)056<0151:TGOMEG>2.0.CO;2, 1999.

Canty, T. P., Hembeck, L., Vinciguerra, T. P., Anderson, D. C., Goldberg, D. L., Carpenter, S. F., Allen, D. J., Loughner, C. P., Salawitch, R. J., and Dickerson, R. R.: Ozone and NO_x chemistry in the eastern US: evaluation of CMAQ/CB05 with satellite (OMI) data, Atmos. Chem. Phys., 15, 10965–10982, https://doi.org/10.5194/acp-15-10965-2015, 2015.

Carlton, A. G., Wiedinmyer, C., and Kroll, J. H.: A review of Secondary Organic Aerosol (SOA) formation from isoprene, Atmos. Chem. Phys., 9, 4987–5005, https://doi.org/10.5194/acp-9-4987-2009, 2009.

Castellanos, P., Boersma, K. F., Torres, O., and de Haan, J. F.: OMI tropospheric NO2 air mass factors over South America: effects of biomass burning aerosols, Atmos. Meas. Tech., 8, 3831–3849, https://doi.org/10.5194/amt-8-3831-2015, 2015.

Chauhan, A., Krishna, M., Frew, A., and Holgate, S.: Exposure to nitrogen dioxide NO_2) and respiratory disease risk, Rev. Environ. Health, 13, 73–90, 1998.

Choi, S., Joiner, J., Choi, Y., Duncan, B. N., Vasilkov, A., Krotkov, N., and Bucsela, E.: First estimates of global free-tropospheric NO_2 abundances derived using a cloud-slicing technique applied to satellite observations from the Aura Ozone Monitoring Instrument (OMI), Atmos. Chem. Phys., 14, 10565–10588, https://doi.org/10.5194/acp-14-10565-2014, 2014.

de Foy, B., Lu, Z., Streets, D. G., Lamsal, L. N., and Duncan, B. N.: Estimates of power plant NO_x emissions and lifetimes from OMI NO_2 satellite retrievals, Atmos. Environ., 116, 1–11, https://doi.org/10.1016/j.atmosenv.2015.05.056, 2015.

Dockery, D. W., Pope, C. A., Xu, X., Spengler, J. D., Ware, J. H., Fay, M. E., Ferris, B. G., and Speizer, F. E.: An Association between Air Pollution and Mortality in Six U.S. Cities, New Engl. J. Med., 329, 1753–1759, https://doi.org/10.1056/nejm199312093292401, 1993.

Emmons, L. K., Walters, S., Hess, P. G., Lamarque, J.-F., Pfister, G. G., Fillmore, D., Granier, C., Guenther, A., Kinnison, D., Laepple, T., Orlando, J., Tie, X., Tyndall, G., Wiedinmyer, C., Baughcum, S. L., and Kloster, S.: Description and evaluation of the Model for Ozone and Related chemical Tracers, version 4 (MOZART-4), Geosci. Model Dev., 3, 43–67, https://doi.org/10.5194/gmd-3-43-2010, 2010.

EPA: Air Pollutant Emissions Trends Data, avalable at: https://www.epa.gov/air-emissions-inventories/air-pollutant-emissions-trends-data, last access: 11 October 2016.

Fujita, E. M., Campbell, D. E., Zielinska, B., Chow, J. C., Lindhjem, C. E., DenBleyker, A., Bishop, G. A., Schuchmann, B. G., Stedman, D. H., and Lawson, D. R.: Comparison of the MOVES2010a, MOBILE6.2, and EMFAC2007 mobile source emission models with on-road traffic tunnel and remote sensing measurements, J. Air Waste Manage., 62, 1134–1149, https://doi.org/10.1080/10962247.2012.699016, 2012.

Goliff, W. S., Stockwell, W. R., and Lawson, C. V.: The regional atmospheric chemistry mechanism, version 2, Atmos. Environ., 68, 174–185, https://doi.org/10.1016/j.atmosenv.2012.11.038, 2013.

Grell, G. A., Peckham, S. E., Schmitz, R., McKeen, S. A., Frost, G., Skamarock, W. C., and Eder, B.: Fully coupled "online" chemistry within the WRF model, Atmos. Environ., 39, 6957–6975, https://doi.org/10.1016/j.atmosenv.2005.04.027, 2005.

Guenther, A., Karl, T., Harley, P., Wiedinmyer, C., Palmer, P. I., and Geron, C.: Estimates of global terrestrial isoprene emissions using MEGAN (Model of Emissions of Gases and Aerosols from Nature), Atmos. Chem. Phys., 6, 3181–3210, https://doi.org/10.5194/acp-6-3181-2006, 2006.

Haagen-Smit, A., Darley, E., Zaitlin, M., Hull, H., and Noble, W.: Investigation on Injury to Plants from Air Pollution in the Los Angeles Area, Plant Physiol., 27, 18–34, 1952.

Hastings, D. and Dunbar, P.: Global Land One-kilometer Base Elevation (GLOBE) Digital Elevation Model, Documentation, Volume 1.0, National Oceanic and Atmospheric Administration, National Geophysical Data Center, 325 Broadway, Boulder, Colorado 80303, USA, 1999.

Heath, R. L.: Responses of plants to air pollution, chap. Ozone, Academic Press, New York, NY, USA; San Francisco, CA, USA; London, United Kingdom, 23–55, 1975.

Hudman, R. C., Jacob, D. J., Turquety, S., Leibensperger, E. M., Murray, L. T., Wu, S., Gilliland, A. B., Avery, M., Bertram, T. H., Brune, W., Cohen, R. C., Dibb, J. E., Flocke, F. M., Fried, A., Holloway, J., Neuman, J. A., Orville, R., Per-

ring, A., Ren, X., Sachse, G. W., Singh, H. B., Swanson, A., and Wooldridge, P. J.: Surface and lightning sources of nitrogen oxides over the United States: Magnitudes, chemical evolution, and outflow, J. Geophys. Res., 112, D12S05, https://doi.org/10.1029/2006JD007912, 2007.

Hudman, R. C., Russell, A. R., Valin, L. C., and Cohen, R. C.: Interannual variability in soil nitric oxide emissions over the United States as viewed from space, Atmos. Chem. Phys., 10, 9943–9952, https://doi.org/10.5194/acp-10-9943-2010, 2010.

Hudman, R. C., Moore, N. E., Mebust, A. K., Martin, R. V., Russell, A. R., Valin, L. C., and Cohen, R. C.: Steps towards a mechanistic model of global soil nitric oxide emissions: implementation and space based-constraints, Atmos. Chem. Phys., 12, 7779–7795, https://doi.org/10.5194/acp-12-7779-2012, 2012.

Huijnen, V., Flemming, J., Kaiser, J. W., Inness, A., Leitão, J., Heil, A., Eskes, H. J., Schultz, M. G., Benedetti, A., Hadji-Lazaro, J., Dufour, G., and Eremenko, M.: Hindcast experiments of tropospheric composition during the summer 2010 fires over western Russia, Atmos. Chem. Phys., 12, 4341–4364, https://doi.org/10.5194/acp-12-4341-2012, 2012.

Izumi, K. and Fukuyama, T.: Photochemical aerosol formation from aromatic hydrocarbons in the presence of NO_x, Atmos. Environ. A-Gen., 24, 1433–1441, https://doi.org/10.1016/0960-1686(90)90052-O, 1990.

Jacob, D. J., Logan, J. A., Gardner, G. M., Yevich, R. M., Spivakovsky, C. M., Wofsy, S. C., Sillman, S., and Prather, M. J.: Factors regulating ozone over the United States and its export to the global atmosphere, J. Geophys. Res., 98, 14817–14826, https://doi.org/10.1029/98JD01224, 1993.

Jiang, Z., McDonald, B. C., Worden, H., Worden, J. R., Miyazaki, K., Qu, Z., Henze, D. K., Jones, D. B. A., Arellano, A. F., Fischer, E. V., Zhu, L., and Boersma, K. F.: Unexpected slowdown of US pollutant emission reduction in the past decade, P. Natl. Acad. Si USA, 115, 5099–5104, https://doi.org/10.1073/pnas.1801191115, 2018.

Jin, Z., Charlock, T. P., Smith, W. L., and Rutledge, K.: A parameterization of ocean surface albedo, Geophys, Res, Lett,, 31, L22301, https://doi.org/10.1029/2004GL021180, 2004.

Jin, Z., Charlock, T., Rutledge, K., Stamnes, K., and Wang, Y.: Analytical solution of radiative transfer in the coupled atmosphere-ocean system with a rough surface, Appl. Optics, 45, 7443–7455, 2006.

Kagawa, J.: Evaluation of biological significance of nitrogen oxides exposure, Tokai J. Exp. Clin. Med., 10, 348, 1985.

Kampa, M. and Castanas, E.: Human health effects of air pollution, Environ. Pollut., 151, 362–367, https://doi.org/10.1016/j.envpol.2007.06.012, 2008.

Kharol, S., Martin, R., Philip, S., Boys, B., Lamsal, L., Jerrett, M., Brauer, M., Crouse, D., McLinden, C., and Burnett, R.: Assessment of the magnitude and recent trends in satellite-derived ground-level nitrogen dioxide over North America, Atmos. Environ., 118, 236–245, https://doi.org/10.1016/j.atmosenv.2015.08.011, 2015.

Krotkov, Nickolay, A. and Veefkind, P.: OMI/Aura Nitrogen Dioxide (NO2) Total and Tropospheric Column 1-orbit L2 Swath 13x24 km V003, Greenbelt, MD, USA, Goddard Earth Sciences Data and Information Services Center (GES DISC), https://doi.org/10.5067/Aura/OMI/DATA2017, 2016.

Krotkov, N. A., Lamsal, L. N., Celarier, E. A., Swartz, W. H., Marchenko, S. V., Bucsela, E. J., Chan, K. L., Wenig, M., and Zara, M.: The version 3 OMI NO2 standard product, Atmos. Meas. Tech., 10, 3133–3149, https://doi.org/10.5194/amt-10-3133-2017, 2017.

Kuhlmann, G., Hartl, A., Cheung, H. M., Lam, Y. F., and Wenig, M. O.: A novel gridding algorithm to create regional trace gas maps from satellite observations, Atmos. Meas. Tech., 7, 451–467, https://doi.org/10.5194/amt-7-451-2014, 2014.

Kurosu, T. P. and Celarier, E. A.: OMI/Aura Global Ground Pixel Corners 1-Orbit L2 Swath 13x24km V003, Greenbelt, MD, USA, Goddard Earth Sciences Data and Information Services Center (GES DISC), https://doi.org/10.5067/Aura/OMI/DATA2020, 2010.

Lamsal, L. N., Martin, R. V., van Donkelaar, A., Steinbacher, M., Celarier, E. A., Bucsela, E., Dunlea, E. J., and Pinto, J. P.: Ground-level nitrogen dioxide concentrations inferred from the satellite-borne Ozone Monitoring Instrument, J. Geophys. Res., 113, D16308, https://doi.org/10.1029/2007JD009235, 2008.

Laughner, J., Zhu, Q., and Cohen, R.: Berkeley High Resolution (BEHR) OMI NO2 – Gridded pixels, daily profiles, v5, UC Berkeley Dash, Dataset, https://doi.org/10.6078/D12D5X, 2018a.

Laughner, J., Zhu, Q., and Cohen, R.: Berkeley High Resolution (BEHR) OMI NO2 – Native pixels, daily profiles, v5, UC Berkeley Dash, Dataset, https://doi.org/10.6078/D1WH41, 2018b.

Laughner, J., Zhu, Q., and Cohen, R.: Berkeley High Resolution (BEHR) OMI NO2 – Gridded pixels, monthly profiles, UC Berkeley Dash, Dataset, https://doi.org/10.6078/D1RQ3G, 2018c.

Laughner, J., Zhu, Q., and Cohen, R.: Berkeley High Resolution (BEHR) OMI NO2 – Native pixels, monthly profiles, UC Berkeley Dash, Dataset, https://doi.org/10.6078/D1N086, 2018d.

Laughner, J. L.: AutoWRFChem-Base v1.2.0: Automation for the WRF-Chem model, Zenodo, https://doi.org/10.5281/zenodo.839040, 2017.

Laughner, J. L. and Cohen, R. C.: Quantification of the effect of modeled lightning NO_2 on UV-visible air mass factors, Atmos. Meas. Tech., 10, 4403–4419, https://doi.org/10.5194/amt-10-4403-2017, 2017.

Laughner, J. L. and Zhu, Q.: Code updated in response to ESSD first reviews, Zenodo, https://doi.org/10.5281/zenodo.1450747, 2018a.

Laughner, J. L. and Zhu, Q.: CohenBerkeleyLab/BEHR-Core: BEHR Core code, Zenodo, https://doi.org/10.5281/zenodo.998275, 2018b.

Laughner, J. L., Zare, A., and Cohen, R. C.: Effects of daily meteorology on the interpretation of space-based remote sensing of NO_2, Atmos. Chem. Phys., 16, 15247–15264, https://doi.org/10.5194/acp-16-15247-2016, 2016.

Laughner, J. L., Zhu, Q., and Cohen, R.: Evaluation of version 3.0B of the BEHR OMI NO_2 product, Atmos. Meas. Tech. Discuss., https://doi.org/10.5194/amt-2018-248, in review, 2018e.

Levelt, P., van der Oord, G., Dobber, M., Mälkki, A., Visser, H., de Vries, J., Stammes, P., Lundell, J., and Saari, H.: The Ozone Monitoring Instrument, IEEE T. Geosci. Remote, 44, 1093–1101, https://doi.org/10.1109/TGRS.2006.872333, 2006.

Lin, J.-T., Liu, M.-Y., Xin, J.-Y., Boersma, K. F., Spurr, R., Martin, R., and Zhang, Q.: Influence of aerosols and surface reflectance

on satellite NO_2 retrieval: seasonal and spatial characteristics and implications for NO_x emission constraints, Atmos. Chem. Phys., 15, 11217–11241, https://doi.org/10.5194/acp-15-11217-2015, 2015.

Liu, F., Beirle, S., Zhang, Q., Dörner, S., He, K., and Wagner, T.: NO_x lifetimes and emissions of cities and power plants in polluted background estimated by satellite observations, Atmos. Chem. Phys., 16, 5283–5298, https://doi.org/10.5194/acp-16-5283-2016, 2016.

Liu, F., Beirle, S., Zhang, Q., van der A, R. J., Zheng, B., Tong, D., and He, K.: NO_x emission trends over Chinese cities estimated from OMI observations during 2005 to 2015, Atmos. Chem. Phys., 17, 9261–9275, https://doi.org/10.5194/acp-17-9261-2017, 2017.

Liu, Y., Bourgeois, A., Warner, T., Swerdlin, S., and Hacker, J.: Implementation of the observation-nudging based on FDDA into WRF for supporting AFEC test operations, 6th WRF Conference, NCAR, Boulder, CO, USA, 2006.

Lorente, A., Folkert Boersma, K., Yu, H., Dörner, S., Hilboll, A., Richter, A., Liu, M., Lamsal, L. N., Barkley, M., De Smedt, I., Van Roozendael, M., Wang, Y., Wagner, T., Beirle, S., Lin, J.-T., Krotkov, N., Stammes, P., Wang, P., Eskes, H. J., and Krol, M.: Structural uncertainty in air mass factor calculation for NO_2 and HCHO satellite retrievals, Atmos. Meas. Tech., 10, 759–782, https://doi.org/10.5194/amt-10-759-2017, 2017.

Lu, Z., Streets, D. G., de Foy, B., Lamsal, L. N., Duncan, B. N., and Xing, J.: Emissions of nitrogen oxides from US urban areas: estimation from Ozone Monitoring Instrument retrievals for 2005–2014, Atmos. Chem. Phys., 15, 10367–10383, https://doi.org/10.5194/acp-15-10367-2015, 2015.

Marais, E. A., Jacob, D. J., Choi, S., Joiner, J., Belmonte-Rivas, M., Cohen, R. C., Beirle, S., Murray, L. T., Schiferl, L., Shah, V., and Jaeglé, L.: Nitrogen oxides in the global upper troposphere: interpreting cloud-sliced NO_2 observations from the OMI satellite instrument, Atmos. Chem. Phys. Discuss., https://doi.org/10.5194/acp-2018-556, in review, 2018.

Marchenko, S., Krotkov, N. A., Lamsal, L. N., Celarier, E. A., Swartz, W. H., and Bucsela, E. J.: Revising the slant column density retrieval of nitrogen dioxide observed by the Ozone Monitoring Instrument, J. Geophys. Res.-Atmos., 120, 5670–5692, https://doi.org/10.1002/2014JD022913, 2015.

Martin, R., Sauvage, B., Folkins, I., Sioris, C., Boone, C., Bernath, P., and Ziemke, J.: Space-based constraints on the production of nitric oxide by lightning, J. Geophys. Res., 112, D09309, https://doi.org/10.1029/2006JD007831, 2007.

McKenzie, R., Johnstone, P., McElroy, C., Kerr, J., and Solomon, S.: Altitude distributions of stratospheric constituents from ground-based measurements at twilight, J. Geophys. Res., 96, 15499–15511, https://doi.org/10.1029/91JD01361, 1991.

McLinden, C. A., Fioletov, V., Boersma, K. F., Kharol, S. K., Krotkov, N., Lamsal, L., Makar, P. A., Martin, R. V., Veefkind, J. P., and Yang, K.: Improved satellite retrievals of NO_2 and SO_2 over the Canadian oil sands and comparisons with surface measurements, Atmos. Chem. Phys., 14, 3637–3656, https://doi.org/10.5194/acp-14-3637-2014, 2014.

Mebust, A. and Cohen, R.: Observations of a seasonal cycle in NO_x emissions from fires in African woody savannas, Geophys. Res. Lett., 40, 1451–1455, https://doi.org/10.1002/grl.50343, 2013.

Mebust, A. K. and Cohen, R. C.: Space-based observations of fire NO_x emission coefficients: a global biome-scale comparison, Atmos. Chem. Phys., 14, 2509–2524, https://doi.org/10.5194/acp-14-2509-2014, 2014.

Mebust, A. K., Russell, A. R., Hudman, R. C., Valin, L. C., and Cohen, R. C.: Characterization of wildfire NO_x emissions using MODIS fire radiative power and OMI tropospheric NO_2 columns, Atmos. Chem. Phys., 11, 5839–5851, https://doi.org/10.5194/acp-11-5839-2011, 2011.

Menzel, D. B.: Ozone: An overview of its toxicity in man and animals, J. Toxicol. Env. Health, 13, 181–204, https://doi.org/10.1080/15287398409530493, 1984.

Miyazaki, K., Eskes, H. J., and Sudo, K.: Global NO_x emission estimates derived from an assimilation of OMI tropospheric NO_2 columns, Atmos. Chem. Phys., 12, 2263–2288, https://doi.org/10.5194/acp-12-2263-2012, 2012.

Miyazaki, K., Eskes, H. J., Sudo, K., and Zhang, C.: Global lightning NO_x production estimated by an assimilation of multiple satellite data sets, Atmos. Chem. Phys., 14, 3277–3305, https://doi.org/10.5194/acp-14-3277-2014, 2014.

Miyazaki, K., Eskes, H., Sudo, K., Boersma, K. F., Bowman, K., and Kanaya, Y.: Decadal changes in global surface NO_x emissions from multi-constituent satellite data assimilation, Atmos. Chem. Phys., 17, 807–837, https://doi.org/10.5194/acp-17-807-2017, 2017.

Myhre, G., Shindle, D., Bréon, F.-M., Collins, W., Fuglestvedt, J., Huang, J., Koch, D., Lamarque, J.-F., Lee, D., Mendoza, B., Nakajima, T., Robock, A., Stephens, G., Takemura, T., and Zhang, H.: Climate Change 2013: The Physical Science Basis, Contribution of Working Group I to the Fifth Assessment Report of the Intergovernmental Panel on Climate Change, edited by: Stocker, T. F., Qin, D., Plattner, G.-K., Tignor, M., Allen, S. K., Boschung, J., Nauels, A., Xia, Y., Bex, V., and Midgley, P. M., Cambridge University Press, Cambridge, United Kingdom and New York, NY, USA, chap.: Anthropogenic and Natural Radiative Forcing, 659–684, 2013.

Nault, B. A., Garland, C., Pusede, S. E., Wooldridge, P. J., Ullmann, K., Hall, S. R., and Cohen, R. C.: Measurements of $CH_3O_2NO_2$ in the upper troposphere, Atmos. Meas. Tech., 8, 987–997, https://doi.org/10.5194/amt-8-987-2015, 2015.

Nault, B. A., Garland, C., Wooldridge, P. J., Brune, W. H., Campuzano-Jost, P., Crounse, J. D., Day, D. A., Dibb, J., Hall, S. R., Huey, L. G., Jimenez, J. L., Liu, X., Mao, J., Mikoviny, T., Peischl, J., Pollack, I. B., Ren, X., Ryerson, T. B., Scheuer, E., Ullmann, K., Wennberg, P. O., Wisthaler, A., Zhang, L., and Cohen, R. C.: Observational Constraints on the Oxidation of NO_x in the Upper Troposphere, J. Phys. Chem. A, 120, 1468–1478, https://doi.org/10.1021/acs.jpca.5b07824, 2016.

Nault, B. A., Laughner, J. L., Wooldridge, P. J., Crounse, J. D., Dibb, J., Diskin, G., Peischl, J., Podolske, J. R., Pollack, I. B., Ryerson, T. B., Scheuer, E., Wennberg, P. O., and Cohen, R. C.: Lightning NO_x Emissions: Reconciling Measured and Modeled Estimates With Updated NO_x Chemistry, Geophys. Res. Lett., 44, 9479–9488, https://doi.org/10.1002/2017GL074436, 2017.

Noel, S., Bovensmann, H., Burrows, J. P., Frerick, J., Chance, K. V., Goede, A. P. H., and Muller, C.: SCIAMACHY instrument on ENVISAT-1, in: Sensors, Systems, and Next-Generation Satellites II, edited by: Fujisada, H., Proc. SPIE, 3498, https://doi.org/10.1117/12.333621, 1998.

Palmer, P., Jacob, D., Chance, K., Martin, R., Spurr, R., Kurosu, T., Bey, I., Yantosca, R., Fiore, A., and Li, Q.: Air mass factor formulation for spectroscopic measurements from satellites: Applications to formaldehyde retrievals from the Global Ozone Monitoring Experiment, J. Geophys. Res., 106, 14539–14550, 2001.

Pandis, S. N., Harley, R. A., Cass, G. R., and Seinfeld, J. H.: Secondary organic aerosol formation and transport, Atmos. Environ. A-Gen., 26, 2269–2282, https://doi.org/10.1016/0960-1686(92)90358-R, 1992.

Parker, L., Kemball-Cook, S., and Yarwood, G.: Final Report Hood County NO_x Trends, Tech. rep., contract #582-16-60185, available at: http://www.hoodcountycleanair.com/userfiles/file/HoodCountyNOxTrends_06Oct2017.pdf (last access: 14 November 2018), 2017.

Pickering, K. E., Bucsela, E., Allen, D., Ring, A., Holzworth, R., and Krotkov, N.: Estimates of lightning NO_x production based on OMI NO_2 observations over the Gulf of Mexico, J. Geophys. Res.-Atmos., 121, 8668–8691, https://doi.org/10.1002/2015JD024179, 2016.

Platnick, S., King, M., Wind, G., Ackerman, S., Menzel, P., and Frey, R.: MODIS/Aqua Clouds 5-Min L2 Swath 1 km and 5 km, NASA MODIS Adaptive Processing System, Goddard Space Flight Center, USA, https://doi.org/10.5067/MODIS/MYD06_L2.006, 2015.

Pope, C. A., Ezzati, M., and Dockery, D. W.: Fine-Particulate Air Pollution and Life Expectancy in the United States, N. Engl. J. Med., 360, 376–386, https://doi.org/10.1056/nejmsa0805646, https://doi.org/10.1056/nejmsa0805646, 2009.

Pusede, S. E., Duffey, K. C., Shusterman, A. A., Saleh, A., Laughner, J. L., Wooldridge, P. J., Zhang, Q., Parworth, C. L., Kim, H., Capps, S. L., Valin, L. C., Cappa, C. D., Fried, A., Walega, J., Nowak, J. B., Weinheimer, A. J., Hoff, R. M., Berkoff, T. A., Beyersdorf, A. J., Olson, J., Crawford, J. H., and Cohen, R. C.: On the effectiveness of nitrogen oxide reductions as a control over ammonium nitrate aerosol, Atmos. Chem. Phys., 16, 2575–2596, https://doi.org/10.5194/acp-16-2575-2016, 2016.

Richter, A. and Wagner, T.: The Use of UV, Visible and Near IR Solar Back Scattered Radiation to Determine Trace Gases, in: The Remote Sensing of Tropospheric Composition from Space, edited by Burrows, J., Platt, U., and Borrell, P., Springer, New York, 2011.

Rollins, A. W., Browne, E. C., Min, K.-E., Pusede, S. E., Wooldridge, P. J., Gentner, D. R., Goldstein, A. H., Liu, S., Day, D. A., Russell, L. M., and Cohen, R. C.: Evidence for NO_x Control over Nighttime SOA Formation, Science, 337, 1210–1212, https://doi.org/10.1126/science.1221520, 2012.

Roujean, J.-L., Leroy, M., and Deschamps, P.-Y.: A bidirectional reflectance model of the Earth's surface for the correction of remote sensing data, J. Geophys. Res., 97, 20455–20468, https://doi.org/10.1029/92JD01411, 1992.

Russell, A. R., Perring, A. E., Valin, L. C., Bucsela, E. J., Browne, E. C., Wooldridge, P. J., and Cohen, R. C.: A high spatial resolution retrieval of NO_2 column densities from OMI: method and evaluation, Atmos. Chem. Phys., 11, 8543–8554, https://doi.org/10.5194/acp-11-8543-2011, 2011.

Russell, A. R., Valin, L. C., and Cohen, R. C.: Trends in OMI NO2 observations over the United States: effects of emission control technology and the economic recession, Atmos. Chem. Phys., 12, 12197–12209, https://doi.org/10.5194/acp-12-12197-2012, 2012.

Schaaf, C. Z. W.: MCD43D07 MODIS/Terra+Aqua BRDF/Albedo Parameter1 Band3 Daily L3 Global 30Arc-Sec CMG V006, NASA EOSDIS Land Processes DAAC, https://doi.org/10.5067/modis/mcd43d07.006, 2015a.

Schaaf, C. Z. W.: MCD43D08 MODIS/Terra+Aqua BRDF/Albedo Parameter2 Band3 Daily L3 Global 30Arc-Sec CMG V006, NASA EOSDIS Land Processes DAAC, https://doi.org/10.5067/modis/mcd43d08.006, 2015b.

Schaaf, C. Z. W.: MCD43D09 MODIS/Terra+Aqua BRDF/Albedo Parameter3 Band3 Daily L3 Global 30Arc-Sec CMG V006, NASA EOSDIS Land Processes DAAC, https://doi.org/10.5067/modis/mcd43d09.006, 2015c.

Schaaf, C. Z. W.: MCD43D31 MODIS/Terra+Aqua BRDF/Albedo QA BRDFQuality Daily L3 Global 30Arc-Sec CMG V006, NASA EOSDIS Land Processes DAAC, https://doi.org/10.5067/modis/mcd43d31.006, 2015d.

Schreier, S. F., Richter, A., Kaiser, J. W., and Burrows, J. P.: The empirical relationship between satellite-derived tropospheric NO_2 and fire radiative power and possible implications for fire emission rates of NO_x, Atmos. Chem. Phys., 14, 2447–2466, https://doi.org/10.5194/acp-14-2447-2014, 2014

Schütt, A.: Improved Gridding Routine of OMI NO_2 data and its applications, Master's thesis, Ludwig-Maximilians-University Munich, 2017.

Schwantes, R. H., Teng, A. P., Nguyen, T. B., Coggon, M. M., Crounse, J. D., St. Clair, J. M., Zhang, X., Schilling, K. A., Seinfeld, J. H., and Wennberg, P. O.: Isoprene NO_3 Oxidation Products from the $RO_2 + HO_2$ Pathway, J. Phys. Chem. A, 119, 10158–10171,https://doi.org/10.1021/acs.jpca.5b06355, 2015.

Slusser, J., Hammond, K., Kylling, A., Stamnes, K., Perliski, L., Dahlback, A., Anderson, D., and DeMajistre, R.: Comparison of air mass computations, J. Geophys. Res., 101, 9315–9321, https://doi.org/10.1029/96JD00054, 1996.

Stahler, A., Lucht, W., Schaaf, C., Tsang, T., Gao, F., Li, X., Muller, J.-P., Lewis, P., Barnsley, M., Strugnell, N., Hu, B., Hyman, A., d'Entremont, R., Chen, L., Liu, Y., McIver, D., Liang, S., Disney, M., Hobson, P., Dunderdale, M., and Roberts, G.: MODIS BRDF/Albedo Product: Algorithm Theoretical Basis Document Version 5.0, 7–15, avalable at: https://lpdaac.usgs.gov/sites/default/files/public/product_documentation/atbd_mod09_v5.pdf (last access: 14 November 2018), 1999.

Travis, K. R., Jacob, D. J., Fisher, J. A., Kim, P. S., Marais, E. A., Zhu, L., Yu, K., Miller, C. C., Yantosca, R. M., Sulprizio, M. P., Thompson, A. M., Wennberg, P. O., Crounse, J. D., St. Clair, J. M., Cohen, R. C., Laughner, J. L., Dibb, J. E., Hall, S. R., Ullmann, K., Wolfe, G. M., Pollack, I. B., Peischl, J., Neuman, J. A., and Zhou, X.: Why do models overestimate surface ozone in the Southeast United States?, Atmos. Chem. Phys., 16, 13561–13577, https://doi.org/10.5194/acp-16-13561-2016, 2016.

Valin, L., Russell, A., and Cohen, R.: "Variations of OH radical in an urban plume inferred from NO_2 column measurements", Geophys. Res. Lett., 40, 1856–1860, https://doi.org/10.1002/grl.50267, 2013.

NO_x van der A, R. J., Eskes, H. J., Boersma, K. F., van Noije, T. P. C., Van Roozendael, M., De Smedt, I., Peters, D. H. M. U., and Meijer, E. W.: Trends, seasonal variability and dominant NO_x source derived from a ten year record of

NO_2 measured from space, J. Geophys. Res., 113, D04302, https://doi.org/10.1029/2007JD009021, 2008.

van Marle, M. J. E., Kloster, S., Magi, B. I., Marlon, J. R., Daniau, A.-L., Field, R. D., Arneth, A., Forrest, M., Hantson, S., Kehrwald, N. M., Knorr, W., Lasslop, G., Li, F., Mangeon, S., Yue, C., Kaiser, J. W., and van der Werf, G. R.: Historic global biomass burning emissions for CMIP6 (BB4CMIP) based on merging satellite observations with proxies and fire models (1750–2015), Geosci. Model Dev., 10, 3329–3357, https://doi.org/10.5194/gmd-10-3329-2017, 2017.

Vasilkov, A., Qin, W., Krotkov, N., Lamsal, L., Spurr, R., Haffner, D., Joiner, J., Yang, E.-S., and Marchenko, S.: Accounting for the effects of surface BRDF on satellite cloud and trace-gas retrievals: a new approach based on geometry-dependent Lambertian equivalent reflectivity applied to OMI algorithms, Atmos. Meas. Tech., 10, 333–349, https://doi.org/10.5194/amt-10-333-2017, 2017.

Veefkind, J., Aben, I., McMullan, K., Förster, H., de Vries, J., Otter, G., Claas, J., Eskes, H., de Haan, J., Kleipool, Q., van Weele, M., Hasekamp, O., Hoogeveen, R., Landgraf, J., Snel, R., Tol, P., Ingmann, P., Voors, R., Kruizinga, B., Vink, R., Visser, H., and Levelt, P.: TROPOMI on the ESA Sentinel-5 Precursor: A GMES mission for global observations of the atmospheric composition for climate, air quality and ozone layer applications, Remote Sens. Environ., 120, 70–83, https://doi.org/10.1016/j.rse.2011.09.027, 2012.

Wanner, W., Li, X., and Strahler, A. H.: On the derivation of kernels for kernel-driven models of bidirectional reflectance, J. Geophys. Res., 100, 21077–21089, https://doi.org/10.1029/95JD02371, 1995.

Wegmann, M., Fehrenbach, A., Heimann, S., Fehrenbach, H., Renz, H., Garn, H., and Herz, U.: NO_2-induced airway inflammation is associated with progressive airflow limitation and development of emphysema-like lesions in C57BL/6 mice, Exp. Toxicol. Pathol, 56, 341–350, https://doi.org/10.1016/j.etp.2004.12.004, 2005.

Zare, A., Romer, P. S., Nguyen, T., Keutsch, F. N., Skog, K., and Cohen, R. C.: A comprehensive organic nitrate chemistry: insights into the lifetime of atmospheric organic nitrates, Atmos. Chem. Phys., 18, 15419–15436, https://doi.org/10.5194/acp-18-15419-2018, 2018.

Zhou, Y., Brunner, D., Boersma, K. F., Dirksen, R., and Wang, P.: An improved tropospheric NO2 retrieval for OMI observations in the vicinity of mountainous terrain, Atmos. Meas. Tech., 2, 401–416, https://doi.org/10.5194/amt-2-401-2009, 2009.

Ziemke, J., Chandra, S., and Bhartia, P.: Cloud slicing: A new technique to derive upper tropospheric ozone from satellite measurements, J. Geophys. Res., 106, 9853–9867, 2001.

Zörner, J., Penning de Vries, M., Beirle, S., Sihler, H., Veres, P. R., Williams, J., and Wagner, T.: Multi-satellite sensor study on precipitation-induced emission pulses of NO_x from soils in semi-arid ecosystems, Atmos. Chem. Phys., 16, 9457–9487, https://doi.org/10.5194/acp-16-9457-2016, 2016.